

¹ **MicroBooNE: Neutron Induced Cosmogenic π^0 's**

² **Ryan A.Grosso**

³ Submitted in partial fulfillment of the
⁴ requirements for the degree
⁵ of Doctor of Philosophy
⁶ in the Graduate School of Arts and Sciences

⁷ **UNIVERSITY OF CINCINNATI**

⁸ 2017

9

10

©2017

11

Ryan A.Grosso

12

All Rights Reserved

¹³ Table of Contents

¹⁴	List of Figures	iii
¹⁵	List of Tables	v
¹⁶	1 Introduction	1
¹⁷	2 Neutrinos & Neutrino Oscillations	3
¹⁸	2.1 The History the Neutrino	3
¹⁹	2.2 Discovery of the Neutrino	5
²⁰	2.3 Neutrinos in the Standard Model	8
²¹	2.4 Neutrino Interactions	9
²²	2.5 Neutrino Mass and Flavor Oscillations	12
²³	2.6 Sterile Neutrinos	17
²⁴	3 The MicroBooNE Detector	18
²⁵	3.1 Brief History of LAR-TPC's	18
²⁶	3.2 Introduction	19
²⁷	3.3 Time Projection Chamber	20
²⁸	3.4 Light Collection	26
²⁹	3.5 Electronics Readout	28
³⁰	4 Booster Neutrino Beam	30
³¹	4.1 Primary Beam, Target and Horn	31
³²	4.2 Neutrino Flux Prediction	32

³³	5 Low Energy Excess and Relevant Cross Sections	35
³⁴	5.1 Overview	35
³⁵	5.2 LSND Excess	35
³⁶	5.3 Miniboone Excess	37
³⁷	5.4 Neutral Current π^0 production	38
³⁸	5.5 NC-Pi0 in Carbon vs Argon	40
³⁹	6 Cosmogenic π^0's at MicroBooNE	41
⁴⁰	6.1 Motivation	41
⁴¹	6.2 Traditional Reconstruction	43
⁴²	6.3 Wire Cell Imaging	44
⁴³	6.4 Pattern Recognition	45
⁴⁴	6.4.1 Clustering	46
⁴⁵	6.5 Track and Shower Selection	48
⁴⁶	6.5.1 Track Removal	48
⁴⁷	6.5.2 Single π^0 Reconstruction	48
⁴⁸	6.6 Single π^0 cosmic sample	52
⁴⁹	7 Results	56
⁵⁰	7.1 Monte Carlo Simulation	56
⁵¹	7.2 Data	59
⁵²	7.3 (.	59
⁵³	8 Conclusions	60
⁵⁴	I Appendices	61

⁵⁵ List of Figures

56	2.1 Cowan and Reines first proposed neutrino experiment.	5
57	2.2 The Hadron production cross section around the Z^0 resonance from LEP.	7
58	2.3 The Standard Model	9
59	2.4 Charge and Neutral Current Interactions	12
60	2.5 This plot shows the appearance and disappearance curves for a 2-flavor ap-	
61	proximation as a function of baseline. The values of $\Delta m^2 = 0.0025\text{eV}^2$ and	
62	$\sin^2 \theta = 0.14$ are used.	14
63	2.6 Neutrino Mass Hierarchy	16
64	3.1 Diagram of a Time Projection Chamber	19
65	3.2 MicroBooNE TPC	21
66	3.3 MicroBooNE wires measured linear mass density	22
67	3.4 Tensioning system	23
68	3.5 Multiple wire planes installed in MicroBooNE	24
69	3.6 MicroBooNE tension measuring device	25
70	3.7 MicroBooNE tension map	26
71	3.8 MicroBooNE tension histogram	26
72	3.9 PMT optical unit	27
73	3.10 PMT optical unit	28
74	3.11 Detector Electronic layout	29
75	4.1 The Booster Neutrino Campus	30
76	4.2 BNB Target	32

77	4.3	Booster Neutrino Beamline	33
78	4.4	BNB Target	34
79	5.1	LSND Excess	36
80	5.2	MiniBooNE Event topology	38
81	5.3	MiniBooNE excess for ν and $\bar{\nu}$	39
82	5.4	pi0production	40
83	6.1	Icarus Cosmic π^0	43
84	6.2	Wire Cell reconstruction of CORSIKA MC viewed in the BEE viewer	46
85	6.3	Shower merging graphic	48
86	6.4	pi0Photon	49
87	6.5	Reconstructed energy sum and energy product for shower pairs. Both, the reconstructed energy sum and product is less than the true energy deposited.	50
89	6.6	pi0Photon	51
90	6.7	pi0Photon	52
91	6.8	pi0Photon	53
92	6.9	Cosmic π^0 production by parent process	54
93	6.10	pi0Photon	55
94	7.1	Enhanced Signal Sample	58
95	7.2	Background Sample	59

List of Tables

97	4.1 Beam Production Systematics	34
98	7.1 Cosiska MC rates	57

⁹⁹ Chapter 1

¹⁰⁰ Introduction

¹⁰¹ This thesis describes work towards electromagnetic shower reconstruction and steps towards
¹⁰² a neutral current single π^0 cross section measurement motivated from reconstruction tech-
¹⁰³ niques used for neutron induced cosmogenic π^0 analysis. This thesis will use data from
¹⁰⁴ the MicroBooNE Liquid Argon Time Projection Chamber(LArTPC) located at the Fermi
¹⁰⁵ National Accelerator in Batavia, Il.

¹⁰⁶

¹⁰⁷ To begin, Chapter 2 will provide some background about the neutrino. We will begin by
¹⁰⁸ presenting the initial premise for the need of a neutrino-like particle. Then, we will describe
¹⁰⁹ the theoretical framework used to address how they interact the standard model. Finally we
¹¹⁰ will present the phenomenon known as neutrino oscillation and provide some mathematical
¹¹¹ framework to describe it. Chapter 3 begins with a brief history of the LArTPC detector
¹¹² technology and its use as a high precision neutrino detector. The chapter continues to
¹¹³ explain in depth the various subsystems that constitute the MicroBooNE detector. Chapter
¹¹⁴ 4 will describe how a neutrino beam is produced and delivered to the MicroBooNE detector.
¹¹⁵ It will focus on Fermilab's Booster Neutrino Beam(BNB) which generates a beam of nearly
¹¹⁶ pure ν_μ or $\bar{\nu}_\mu$ around 1GeV in average energy. Chapter 5 will present in detail the claims
¹¹⁷ of the electromagnetic ν_e -like excess first seen by the LSND experiment and then later
¹¹⁸ verified by the MiniBooNE experiment. This chapter will also discuss the neutral current
¹¹⁹ cross section, which is the main background in the MiniBooNE excess claim. Chapter
¹²⁰ 6 will introduce MicroBooNE's cosmogenic background and motivate the importance of

understanding the cosmic rate. Here, we will also discuss the motivation to use cosmic π^0 events as a means of calibrating the detector energy scale. The cosmic backgrounds are addressed for the oscillation analysis and a future neutral current 1 π^0 measurement. Next, this chapter will address simulation, reconstruction, and event selection. Chapter 7 will present results from MicroBooNE cosmics data addressing the cosmic π^0 rate from neutral induced events.

Chapter 2

Neutrinos & Neutrino Oscillations

2.1 The History the Neutrino

The story of the neutrino began in Paris on a cloudy winter day in the year 1896. Parisian native, Henri Becquerel was experimenting with uranium salts and investigating the newly discovered x-ray radiation. [] He hypothesized that when the salts were energized by sunlight they would produce the x-ray radiation. This hypothesis was disproven on the cloudy February 27th day when his experiment still detected radiation emitting from the salts in the absence of the sun. Becquerel had discovered radioactivity. In the coming years, this phenomena was supported by the work of Marie and Pierre Curie in studying the radioactivity of the element Thorium which lead to their discovery of the elements Polonium and Radium. These discoveries would later win Becquerel and the Currie's the 1903 Nobel Prize in Physics.

140

After radioactivity became an accepted phenomena in the science community, Ernst Rutherford discovered that radioactive decay products came in two different forms. He labeled them as α -decay and β -decay. At the time, beta decay was believed to be a two body decay where a nucleus A decays into a lighter nucleus A' and a β -particle(electron). The outgoing energy of the electron from a two body decay is given by equation 2.1. Assuming conservation of energy, the value of the outgoing energy should be a discrete.

$$E_e = \frac{m_A^2 + me^2 - m_{A'}^2}{2m_A} \quad (2.1)$$

147 In 1914, James Chadwick had discovered that the energy spectrum of the β -particles
 148 were continuations as opposed to mono-energetic. While some scientist were willing to
 149 abandon the requirement of energy conservation, others found this to be an unpalatable
 150 solution. Unable to attend the 1930 Tubingen physics conference in Germany, Wolfgang
 151 Pauli wrote a letter to the attendees in which he proposed the first idea of the neutrino.
 152 An excerpt from his famous December 4th letter is translated from German below [].

153 I have hit upon a desperate remedy to save the “exchange theorem” of statistics
 154 and the law of conservation of energy. Namely, the possibility that there could
 155 exist in the nuclei electrically neutral particles, that I wish to call neutrons,
 156 which have spin 1/2 and obey the exclusion principle and which further differ
 157 from light quanta in that they do not travel with the velocity of light. The
 158 mass of the neutrons should be of the same order of magnitude as the electron
 159 mass and in any event not larger than 0.01 proton masses. The continuous beta
 160 spectrum would then become understandable by the assumption that in beta
 161 decay a neutron is emitted in addition to the electron such that the sum of the
 162 energies of the neutron and the electron is constant...

163 In 1932, Chadwick discovered the neutron we know of today. Unfortunately, this neutron
 164 was too heavy to be the particle that Pauli had proposed. Expanding on Pauli’s work, Enrico
 165 Fermi proposed a more complete picture of beta decay and renamed Pauli’s ‘neutron’ to
 166 what is commonly called a *neutrino*. Fermi’s theory directly coupled the neutron with a
 167 final state proton, electron, and neutrino. This theory of beta decay, $n \rightarrow p + e^- + \bar{\nu}_e$
 168 preserves the law of conservation of energy and would later prove to be a more accurate
 169 descriptor of the process.

¹⁷⁰ **2.2 Discovery of the Neutrino**

¹⁷¹ Measuring and detecting neutrinos is a tricky business. In the 1950's, Clyde Cowan and
¹⁷² Frederick Reines set out to directly measure neutrino interactions for the first time. If a free
¹⁷³ neutrino existed, they hypothesized that they could detect the byproducts from the inverse
¹⁷⁴ beta decay $\bar{\nu}_e + p \rightarrow e^+ + n$. They realized that such a measurement would require a very
¹⁷⁵ intense neutrino source and a large detector. Their first proposal, which was approved, was
¹⁷⁶ to detonate a nuclear bomb to supply the large, instantaneous source of neutrinos. A large
¹⁷⁷ detector filled with liquid scintillator would free fall down a mind shaft recording flashes
¹⁷⁸ of light from the ionizing positrons before landing on a bed of feathers and foam rubber.
¹⁷⁹ The original experimental schematic is shown in Figure 2.1. At that time, the theorized
¹⁸⁰ neutrino cross section was $10^{-43} \text{ cm}^2/\text{proton}$ while the existing measured limit was still 7
¹⁸¹ orders of magnitude short in sensitivity. The bomb experiment would have worked but
¹⁸² could not provide the level of sensitivity required to confirm detection for neutrino cross
¹⁸³ sections below $10^{-39} \text{ cm}^2/\text{proton}$. This was due to background interactions that came in
¹⁸⁴ time directly from the bomb.

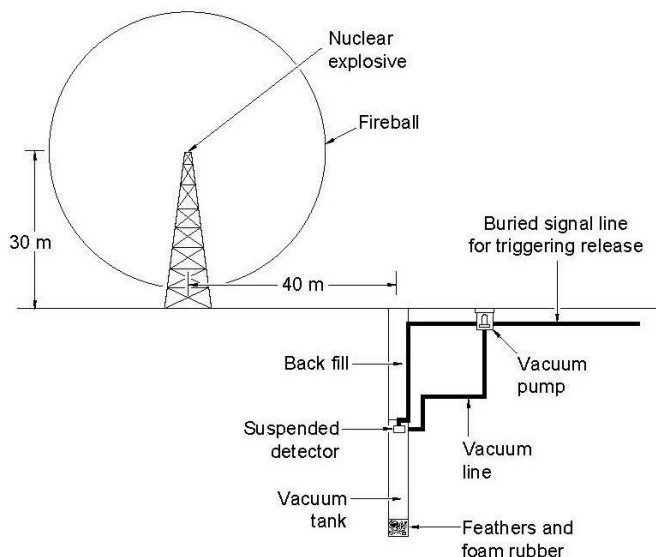
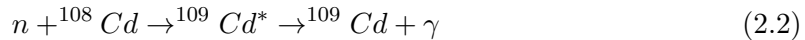


Figure 2.1: Original sketch of Cowan and Reines first proposed neutrino experiment.

Later, Reines realized tagging both the positron and neutron through a double coincidence would drastically reduce the backgrounds. This meant they could use a less intense neutrino source such as a nuclear reactor. They chose the Savannah River Plant near Augusta, Georgia which was estimated to produce neutrino fluxes on the order of $10^{12} - 10^{13}$ neutrinos/s/cm². The detector was composed of a water target that was doped with CdCl₂. As stated prior, the signal would rely on a double coincidence flash measured from photomultipiler tubes inside their detector. First, they would detect the positron as it annihilates with an electron via pair production ($e^+ + e^- \rightarrow \gamma + \gamma$). This is identified by two, back-to-back, coincident 0.511 MeV photons. Then, approximately 5μS later, a secondary photon would be detected which was produced from the neutron capture on Cadmium as shown in equation 2.2.



In 1956, only 25 years after Pauli's initial proposal of the neutrino, Cowan and Reines succeeded and provided the first direct experimental evidence of the electron flavor neutrino. In the subsequent years, the existence of two other flavors of neutrinos have been verified. In 1962, Lederman, Schwartz, and Steinberger discovered the ν_μ at Brookhaven Nation Laboratory by measuring neutrinos coming from pion decay. The ν_μ would be distinctly different from that of ν_e if the process $\nu_\mu + n \rightarrow p + e^-$ was forbidden. The results showed that the neutrinos from pion decay were indeed muon-like. Finally in 2000, the DONUT(Direct Observation of NeUtrino Tau) experiment stationed at Fermilab, made the first observed measurement of the ν_τ .

In 1956, C.S. Wu had shown that outgoing electron from beta decay maintained an opposing spin with respect to the spin of the parent nucleus. This turned out to be the first proof of maximal parity violation in weak interactions. Shortly thereafter, the neutrino helicity was first measured at Brookhaven National Labs by Maurice Goldhaber. In nature, neutrinos only have left handed helicity, while anti-neutrinos have right handed helicity. Helicity is frame dependent for particles with mass, which means there can be a reference frame in which the momentum vector can switch but the spin vector will not. For a

mass zero particles, this is not possible because the particle would already be traveling at the speed of light. This assumption is what lead to the believe that neutrinos were massless.

The number of active light neutrinos are well constrained by studying the decay of the Z^0 boson at LEP(Large Electron-Positron collider). LEP was an electron-positron collider ring with a circumference of approximately 27 km that supported four primary experiments (L3, ALEPH, OPAL and DELPHI). The facility was coined the phrase “Z-Factory” due to it’s ability to record approximately 1000 Z^0 boson decays every hour during optimal running conditions. The number of active neutrinos, N_ν is related to the width of the Z^0 resonance. Using 17 million Z^0 decays, LEP was able to show that $N_\nu = 2.9840 \pm 0.0082$

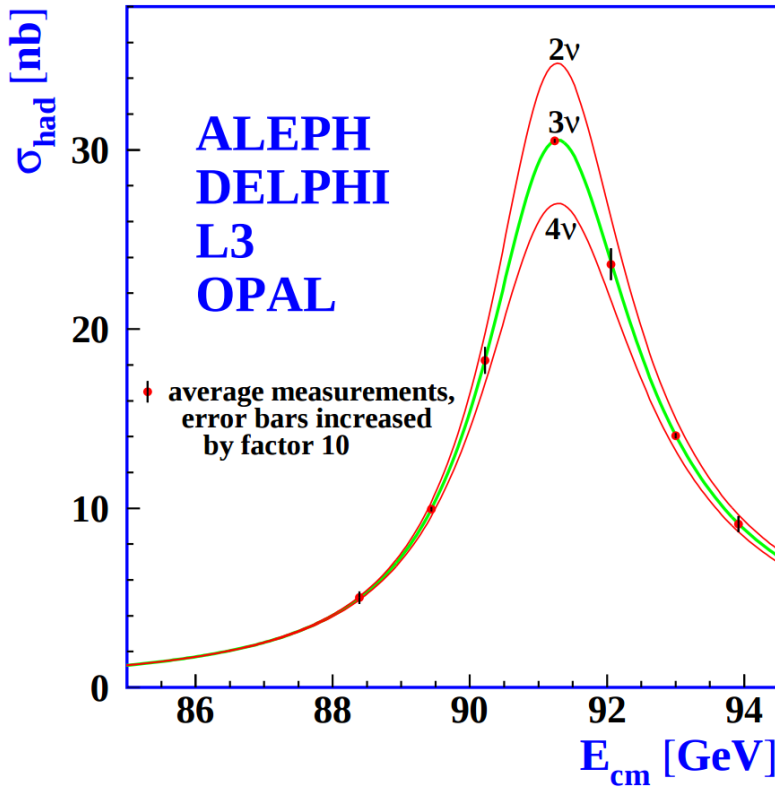


Figure 2.2: The Hadron production cross section around the Z^0 resonance from LEP. The curves for two, three, and four neutrino flavors are shown. The fit shows very compelling evidence of three active flavors of neutrinos.

221 2.3 Neutrinos in the Standard Model

222 In the later half of the 20th century, scientists were looking for a way to describe all the
223 fundamental forces and classify the known particles. The standard model of particle physics
224 is a phenomenological framework that describes the interaction of fundamental particles be-
225 tween the strong and electroweak forces. Having stood the test of time, the standard model
226 accurately predicts most elementary particle interactions, but, does have it's limitations.
227 The standard model does not account for gravity nor does it account for many new physics
228 issues such as dark matter or dark energy. Most importantly, as we will see in section 2.5,
229 it does not provide an accurate description of the neutrino.

230 The standard model consists of two types of particles, bosons and fermions. The funda-
231 mental bosons consist of two families: gauge bosons, which are typically the force carriers,
232 and scalar bosons, which refer to spin zero particles or fields. The gluon, photon, and the
233 weak boson are gauge bosons that mediate the strong, electromagnetic, and weak forces,
234 respectively. The Higgs boson is a scalar boson that possesses a nonzero vacuum expec-
235 tation value of 246GeV . This provides a mechanism for certain particles to gain mass
236 even though their symmetries would suggest zero mass. The fundamental fermions are also
237 divided into two families, quarks and leptons each having three generations. The quarks
238 compose two main categories of particles, baryons and mesons. Baryons consist of an en-
239 semble of 3 quarks. The most common and stable baryons in the universe are protons(uud)
240 and neutrons(udd). Meson consist of an ensemble of quark anti-quark pairs and tend to
241 have shorter lifetimes than their corresponding baryons. The lightest and most common
242 mesons are pions($u\bar{d}, d\bar{u}, u\bar{u}/d\bar{d}$) and kaons($u\bar{s}, s\bar{u}, d\bar{s}/s\bar{d}$). The leptons are also divided into
243 two families with three generations each. The charged leptons, most notably the electron,
244 interact via the strong and weak nuclear force and combine to form common baryonic mat-
245 ter. The neutral leptons are the neutrinos and only interact via the weak nuclear force.
246 More details such as, mass, charge, and spin for various particles are shown in figure 2.3

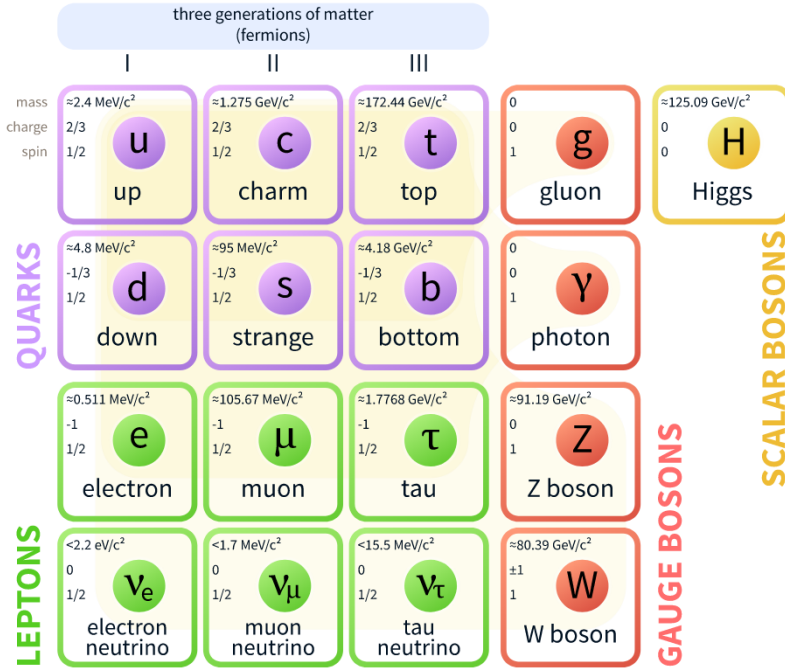


Figure 2.3: The current view of the standard model.

247 2.4 Neutrino Interactions

248 Neutrinos interact via the weak force. In the standard model, the weak force is unified
 249 with the electromagnetic force through an $SU(2) \otimes U(1)$ symmetry. The structure of the
 250 $SU(2)$ group symmetry accounts for the chirality of the fermion fields, along with ability to
 251 produce massive gauge bosons. The $U(1)$ group symmetry accounts for the massless photon
 252 propagator needed for electromagnetic interactions. For the quark and fermion families we
 253 define fermion fields in equations 2.3 and 2.4 , respectively. For formality we will define
 254 right(left)- handed neutrino(anti-neutrino) fields knowing that they will become irrelevant
 255 as the theory evolves:

$$\psi_1(x) = \begin{pmatrix} q \\ q' \end{pmatrix}_L, \quad \psi_2 = q_R, \quad \psi_3 = q'_R \quad (2.3)$$

$$\psi_1(x) = \begin{pmatrix} \nu \\ l \end{pmatrix}_L, \quad \psi_2 = \nu_R, \quad \psi_3 = l_R \quad (2.4)$$

256 We begin with the free Lagrangian, defined in equation 2.5, as it is already invariant in
 257 flavor space.

$$\mathcal{L}_{\text{free}} \equiv \bar{\psi}(i\cancel{\partial} - m)\psi = i\bar{\psi}(x)\gamma^\mu\partial_\mu\psi(x) - m\bar{\psi}(x)\psi(x) \quad (2.5)$$

258 To make the Lagrangian invariant under local $SU(2) \otimes U(1)$, the fermion derivatives
 259 have to be changed to covariant objects. This produces 4 different gauge parameters, shown
 260 in equations 2.6, which correspond to the 4 different gauge fields required to describe the
 261 W^\pm , Z^0 , and γ .

$$\begin{aligned} D_\mu\psi_1(x) &\equiv [\partial_\mu - ig\widetilde{W}_\mu(x) - ig'y_1B_\mu(x)]\psi_1(x) \\ D_\mu\psi_2(x) &\equiv [\partial_\mu - ig'y_2B_\mu(x)]\psi_2(x) \\ D_\mu\psi_3(x) &\equiv [\partial_\mu - ig'y_3B_\mu(x)]\psi_3(x) \end{aligned} \quad (2.6)$$

262 Where, σ^i are the Pauli spin matrices and B_μ represents a field imposed by an external
 263 source. We find that,

$$\begin{aligned} \widetilde{W}_\mu(x) &\equiv \frac{\sigma_i}{2} \left\{ \partial_\mu W_\nu^i - \partial_\nu^i + g\epsilon^{ijk}W_\mu^jW_\nu^k \right\} \\ B_{\mu\nu} &\equiv \partial_\mu B_\nu - \partial_\nu B_\mu \end{aligned} \quad (2.7)$$

264 The Lagrangian now satisfies $SU(2) \otimes U(1)$ symmetry between all gauge fields as shown
 265 in equation 2.8. It should be noted that the fermion fields and gauge bosons are required to
 266 be massless. This does not accurately describe the true interaction since 3 of the 4 gauge
 267 bosons are known to have mass, but the theory does allow an interface between neutrino
 268 interactions in the standard model.

$$\mathcal{L} = \sum_{j=0}^3 i\bar{\psi}_j(x)\gamma^\mu D_\mu\psi_j(x) \quad (2.8)$$

269 From equation 2.8, the terms that account for interaction of gauge bosons with the
 270 fermion fields are shown below in equation 2.9

$$\mathcal{L} \rightarrow g\bar{\psi}_1(x)\gamma^\mu\widetilde{W}_\mu\psi_1(x) + g'B_\mu\sum_{j=0}^3 y_j\bar{\psi}_j(x)\gamma^\mu\psi_j(x) \quad (2.9)$$

271 From this, we are then able to construct the Lagrangian for both the charged and neutral
 272 currents. The charge current Lagrangian is shown in equation 2.10.

$$\mathcal{L}_{CC} = \frac{g}{2\sqrt{2}} \left\{ W_\mu^\dagger [\bar{q}\gamma^\mu(1-\gamma_5)q' + \bar{\nu}\gamma^\mu(1-\gamma_5)\bar{l}] + \dots \right\} \quad (2.10)$$

273 The neutral current term in the Lagrangian contains gauge fields for both the Z boson
 274 and photon, which can be broken into two terms to account for a non-zero Z boson mass
 275 while leaving the photon massless through spontaneous symmetry breaking(SSB). This is
 276 done through an arbitrary rotation, as shown in equation 2.11, where θ_w is known as the
 277 Weinberg or weak mixing angle. This angle is important because it is the angle used to
 278 rotate through SSB giving the Z boson its mass.

$$\begin{pmatrix} W_\mu^3 \\ B_\mu \end{pmatrix} = \begin{pmatrix} \cos \theta_w & \sin \theta_w \\ -\sin \theta_w & \cos \theta_w \end{pmatrix} \times \begin{pmatrix} Z_\mu \\ A_\mu \end{pmatrix} \quad (2.11)$$

279 It is then possible to write the neutral current Lagrangian that accounts for the inter-
 280 action of the Z boson as shown in equation 2.13.

$$\mathcal{L}_{NC} = \frac{e}{2\sin(\theta_w)\cos(\theta_w)} Z_\mu \sum_f \bar{f}\gamma^\mu(v_f - \alpha_f\gamma_5)f \quad (2.12)$$

281 where,

$$g\sin(\theta_w) = g'\cos(\theta_w) = e \quad \text{and} \quad \cos(\theta_w) = \frac{M_w}{M_z} \quad (2.13)$$

282 The neutral current coupling constants, v_f & α_f , differ with respect to the various quark,
 283 charged and neutral lepton fields. The neutrinos can be described as interactions via the
 284 charged and neutral currents. The Feynman diagrams, shown in figure 2.4, depict how the
 285 leptons couple to the quarks via the current mediator.

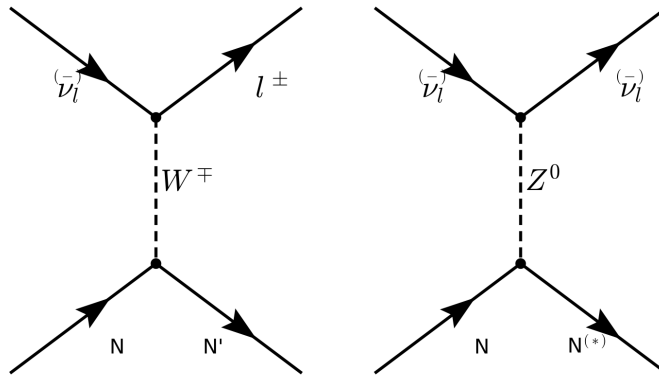


Figure 2.4: The Feynman diagram on the left describes a charged current(CC) neutrino interaction which transforms neutrinos into their corresponding charged leptons. In the CC interaction diagram the $N \rightarrow N'$ represents a changed nucleon charge. The diagram on the right shows the neutral current(NC) neutrino interaction with preserves the neutrino while it interacts. In the NC interaction diagram the $N \rightarrow N^*$ represents a same charge nucleon that could be at a higher resonance state.

2.5 Neutrino Mass and Flavor Oscillations

Neutrino oscillation is a quantum mechanical phenomenon in which the fraction of neutrino flavor changes while it propagates. This phenomena was first proposed in 1957 by Bruno Pontecorvo and relates the neutrino mass eigenstates with the flavor eigenstates through a rotation. This phenomena is best shown through a two neutrino flavor example, then extended into 3 flavors.

The mixing matrix for a two flavor neutrino case is:

$$\begin{pmatrix} \nu_e \\ \nu_\mu \end{pmatrix} = \begin{pmatrix} \cos \theta & \sin \theta \\ -\sin \theta & \cos \theta \end{pmatrix} \begin{pmatrix} \nu_1 \\ \nu_2 \end{pmatrix} \quad (2.14)$$

In this example, the flavor states are represented as ν_e and ν_μ which are expressed as a mixture of mass states ν_1 and ν_2 . For ascetic reasons, we chose ν_μ to be part of the example because most man made neutrino beams produce a relative pure sample of ν_μ . The framework for this example is commonly used as an oscillation approximation and can be generalized to satisfy any case of two distinctly different flavor neutrinos.

298 Using the two flavor formalism a pure ν_μ neutrino state can be expressed as equation
 299 2.15

$$|\nu_\mu(0)\rangle = -\sin \theta |\nu_1(0)\rangle + \cos \theta |\nu_2(0)\rangle \quad (2.15)$$

300 The evolution of the state is governed by solving the time dependent Schroedinger
 301 equation for the initial muon state:

$$|\nu_\mu(t)\rangle = e^{-i\frac{Et}{\hbar}} |\psi(0)\rangle = -e^{-i\frac{E_1 t}{\hbar}} \sin \theta |\nu_1\rangle + e^{-i\frac{E_2 t}{\hbar}} \cos \theta |\nu_2\rangle \quad (2.16)$$

302 Assuming neutrinos travel near the speed of light, we rewrite equation 2.16 using the
 303 relativistic approximation, along with setting $c = \hbar = 1$ and $p_1 = p_2 = p$:

$$|\nu_\mu(t)\rangle \simeq -e^{-i(p_1 + \frac{m_1^2}{2p_1})t} \sin \theta |\nu_1\rangle + e^{-i(p_2 + \frac{m_2^2}{2p_2})t} \cos \theta |\nu_2\rangle \quad (2.17)$$

304 with,

$$E = \sqrt{p^2 + m^2} = p \sqrt{1 + \frac{m^2}{p^2}} \approx p + \frac{m^2}{2p} \quad (2.18)$$

305 Next, the mass terms are grouped together and defined as the absolute square difference,
 306 $\Delta m^2 \equiv |m_2^2 - m_1^2|$. We find that if the mass are different then the mass eigenstates propagate
 307 at different frequencies and give rise the oscillatory behavior. The time dependent state can
 308 now be wrote as:

$$|\nu_\mu(t)\rangle = e^{-i\phi} (-\sin \theta |\nu_1\rangle + e^{+i\frac{\Delta m^2}{2p}t} \cos \theta |\nu_2\rangle) \quad (2.19)$$

with, $e^{-i\phi} \equiv e^{-i\left(p + \frac{m_1}{2p}\right)t}$

309 To calculate the probability of the initial ν_μ state being measured as a ν_e state at some
 310 later time t , we need to calculate the absolute value squared of the overlap between the
 311 states. Utilizing the relationship $\langle \psi_i | \psi_j \rangle = \delta_{i,j}$, the overlap between the states is:

$$\langle \nu_e | \nu_\mu(t) \rangle = e^{-i\phi} (-\sin \theta \cos \theta + \sin \theta \cos \theta e^{i\frac{\Delta m^2}{2p}t}) \quad (2.20)$$

³¹² The probability reduces to:

$$\begin{aligned}
 P(\nu_\mu \rightarrow \nu_e) &= |\langle \nu_e | \nu_\mu(t) \rangle|^2 \\
 &= e^{i\phi} e^{-i\phi} \sin^2 \theta \cos^2 \theta (-1 + e^{-i\frac{\Delta m^2}{p}t})(-1 + e^{+i\frac{\Delta m^2}{p}t}) \\
 &= \frac{1}{2} \sin^2 2\theta \left(1 - \cos \left(\frac{\Delta m^2}{2p} t \right) \right)
 \end{aligned} \tag{2.21}$$

³¹³ Finally, from relativistic assumptions, we set $p = E_\nu$ as the outgoing neutrino energy
³¹⁴ and $t = L$ corresponds to the distance traveled.

$$P(\nu_\mu \rightarrow \nu_e) = \sin^2 2\theta \sin^2 \left(\frac{\Delta m^2 L}{4E_\nu} \right) \tag{2.22}$$

³¹⁵ From a proper accounting of numerical values of c and \hbar , equation 2.26 is more com-
³¹⁶ monly written as:

$$P(\nu_\mu \rightarrow \nu_e) = \sin^2 2\theta \sin^2 \left(1.27 \frac{\Delta m^2 L}{E_\nu} \right) \tag{2.23}$$

³¹⁷ This oscillation behavior is best visualized as a plot of the probability of appearance
³¹⁸ and disappearance as shown Figure 2.5.

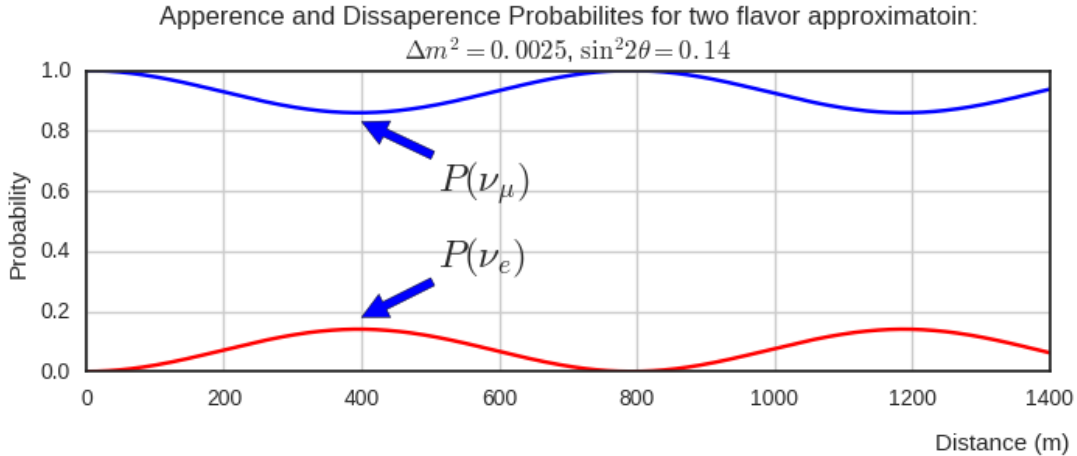


Figure 2.5: This plot shows the appearance and disappearance curves for a 2-flavor approximation as a function of baseline. The values of $\Delta m^2 = 0.0025 \text{ eV}^2$ and $\sin^2 \theta = 0.14$ are used.

As shown prior from figure 2.2, there are very good constraints on the number of active neutrinos. Extending this formalism to a 3 flavor case was done by Pontecorvo-Maki-Nakagawa-Sakata (PMNS). The PMNS matrix is a 3 dimensional unitary matrix which is parameterized by three mixing angles $\theta_{12}, \theta_{23}, \theta_{13}$ a complex phase δ . The three angle correspond to the mixing effect, while δ is known as the charge parity(CP) phase. If the CP-phase is non-zero, then neutrinos violate charge parity conservation which leads to the conclusion that neutrinos and anti-neutrinos interact differently with matter. The value for δ has yet to be observed.

$$U_{PMNS} = \begin{pmatrix} 1 & 0 & 0 \\ 0 & c(\theta_{23}) & s(\theta_{23}) \\ 0 & -s(\theta_{23}) & c(\theta_{23}) \end{pmatrix} \begin{pmatrix} c(\theta_{13}) & 0 & s(\theta_{13})e^{-i\delta} \\ 0 & 1 & 0 \\ -s(\theta_{13})e^{i\delta} & 0 & c(\theta_{13}) \end{pmatrix} \begin{pmatrix} c(\theta_{12}) & s(\theta_{12}) & 0 \\ -s(\theta_{12}) & c(\theta_{12}) & 0 \\ 0 & 0 & 1 \end{pmatrix} \quad (2.24)$$

where $c(\theta_{ij}) \equiv \cos \theta_{ij}$ and $s(\theta_{ij}) \equiv \sin \theta_{ij}$. The matrix equation is now put into a more compact manor that relates the mixing of the 3 neutrino generations.

$$\begin{pmatrix} \nu_e \\ \nu_\mu \\ \nu_\tau \end{pmatrix} = \begin{pmatrix} U_{e,1} & U_{e,2} & U_{e,3} \\ U_{\mu,1} & U_{\mu,2} & U_{\mu,3} \\ U_{\tau,1} & U_{\tau,2} & U_{\tau,3} \end{pmatrix} \begin{pmatrix} \nu_1 \\ \nu_2 \\ \nu_3 \end{pmatrix} \quad (2.25)$$

In it's most general form, the oscillation probability is:

$$P(\nu_\alpha \rightarrow \nu_\beta) = \delta_{\alpha,\beta} - 4 \sum_{j>i} U_{\alpha,i} U_{\beta,i} U_{\alpha,j}^* U_{\beta,j}^* \sin^2 \left(1.27 \frac{\Delta m_{ij}^2 L}{E_\nu} \right) \quad (2.26)$$

From equation 2.26, we see that the oscillation probability is depended on the mass difference between states. There is currently no method to directly measure the mass of any given neutrino. Therefore, there is an allowed ambiguity in the mass ordering of all three neutrino states. This is called the neutrino hierarchy problem. However, we do know that the difference between m_1 and m_2 is small relative to m_3 . Using this, we can build a picture of the fraction of different flavor eigenstates corresponding to their various mass states for both types of hierarchy.

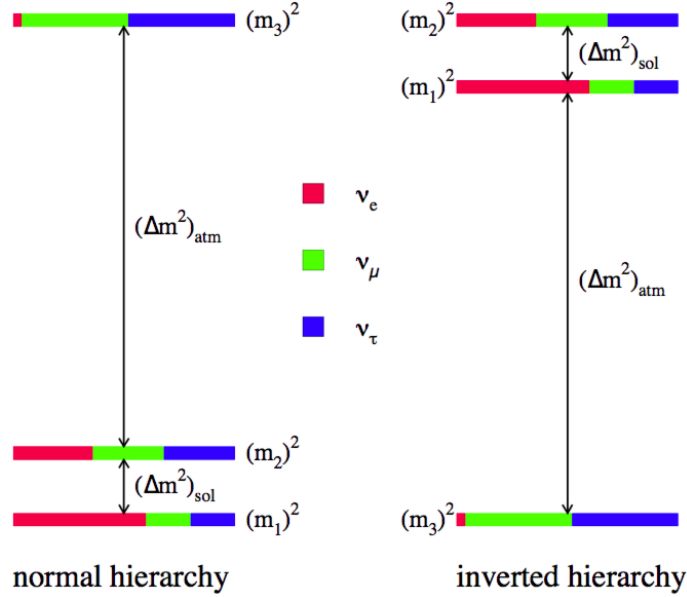


Figure 2.6: The two possible ordering for the 3 active neutrino mass eigenstates.

Many experiments have measures various elements of the PMNS matrix with neutrinos coming from accelerators, reactors, and solar sources. Currently, normal hierarchy ($m_1 < m_2 < m_3$) is favored, therefore we will show (table 2.27) the current Particle Data Group(PDG) best fit values for oscillation parameters with respect to normal hierarchy.

$$\begin{aligned}
 \Delta m_{21}^2 &= 7.37 \times 10^{-5} eV^2 \\
 \Delta m_{32}^2 &= 2.50 \times 10^{-3} eV^2 \\
 \sin(\theta_{12}) &= 0.297 \\
 \sin(\theta_{23}) &= 0.437 \\
 \sin(\theta_{13}) &= 0.0214 \\
 \delta/4 &= 1.35
 \end{aligned} \tag{2.27}$$

³⁴¹ 2.6 Sterile Neutrinos

³⁴² It is well accepted, from measurements at LEP[], that there are only 3 neutrinos that couple
³⁴³ through the weak interaction. Mathematically, nothing prohibits a theory that allows for
³⁴⁴ neutrino mixing with other neutrino states beyond the 3 active states. These states, since
³⁴⁵ they do not interact weakly, are called 'sterile neutrinos'. Extending the 3 flavor oscillation
³⁴⁶ model to include any number of sterile neutrinos may be a possibility to address some the
³⁴⁷ currently unexplained results in the neutrino physics fields. Each additional state requires
³⁴⁸ an extra dimension to be added to the PMNS matrix. The sterile eigenstates are then
³⁴⁹ defined as

$$|\nu_{s_i}\rangle = \sum_j^{3+N} U_{s_i,j} |\nu_j\rangle \quad (2.28)$$

³⁵⁰ where N is the number of sterile neutrinos. The necessity for additional sterile neutrinos
³⁵¹ was prompted by the LSND experiment and later supported by the MiniBooNE. experiment.
³⁵² Both experiments are explained in depth in chapter 5. Each experiment found an excess
³⁵³ of electron-like events at low energy. This suggested a Δm^2 parameter space observed to
³⁵⁴ be 1eV^2 larger than expected and strongly contradicted the results of many other results
³⁵⁵ which had Δm^2 around $\mathcal{O}(10^{-3}\text{eV}^2)$ and $\mathcal{O}(10^{-5}\text{eV}^2)$. This precipitated the need for
³⁵⁶ further exploration of the LSND and MiniBooNE claims with more sophisticated detector
³⁵⁷ technologies. The MicroBooNE experiment was proposed in 2007¹ and will be the focal
³⁵⁸ point for this thesis.

359 Chapter 3

360 The MicroBooNE Detector

361 3.1 Brief History of LAr-TPC's

362 The surprising nature of neutrinos quickly prompted the need for precision measurements
363 of their interactions. Unfortunately, the low neutrino cross section posed a hurdle to build
364 a high statistics detector. In 1977, C.Rubbia propose a Liquid Argon Time Projection
365 Chamber (LArTPC) as large, high precision neutrino detector.^[1] In 2001, The ICARUS col-
366 laboration commissioned the T600 detector which was one of the first large scale LArTPC's
367 to be used as a neutrino detector. ^[2] The T600, which is comprised 760 tons of liquid argon
368 and commissioned in Pavia, Italy using cosmic rays as a proof of principle. Later the T600
369 was place underground in Hall B of Laboratori Nazionali del Gran Sasso (LNGS) which is
370 located 730 km from the source of the CERN neutrino beam.

371 In 2009, the AgroNeut collaboration, commissioned a small LArTPC in a 175 liter
372 vacuum jacketed cryostat. The ArgoNeut TPC was comprised of 3 wire planes and operated
373 at a drift field of 500 V/cm. The detector was placed just in front of the MINOS near
374 detector in the NuMI beam at Fermi National Accelerator Laboratory(FNAL)^[3]. AgroNeut
375 collected thousands of neutrino and antineutrino events providing valuable physics data and
376 detector R&D for future experiments with LArTPC's.

377 The MicroBooNE (the Micro Booster Neutrino Experiment) detector, which will be
378 discussed in depth throughout this chapter, is the first multi-ton LArTPC to be fully op-
379 erational in the U.S. The MircoBooNE detector design pioneered many new detector R&D

concepts such as: the ability to maintain high LAr purity in an unevaluated vessel, implementation of low noise electronic readouts at liquid cryogenic temperatures and advances in reconstruction techniques. MicroBooNE also, supports a robust, high statistics physics program to address the MiniBooNE Low Energy Excess and various cross section measurements. MicroBooNE was commissioned and began taking cosmic ray data in the summer of 2015. In October 2015 it began taking neutrino data. Shortly there after, the first neutrino event candidates were identified. []

3.2 Introduction

The MicroBooNE detector utilizes 170 tons of liquid argon to sustain 87 tons of active detector mass. It is located at the Liquid Argon Test Facility (LARTF) which is 470 m downstream of the Booster Neutrino Beam-line(BNB) source at the Fermilab National Accelerator Lab (FNAL) in Batavia, Illinois. The detector is the first large scale LArTPC to be deployed, commissioned and fully operated in the US.

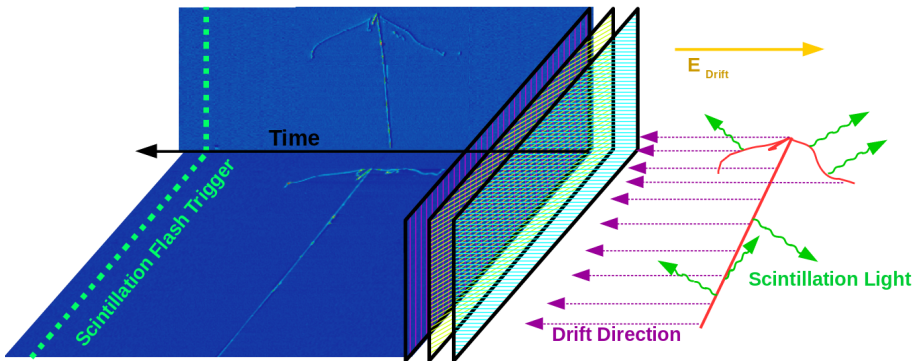


Figure 3.1: This diagram explains how a TPC works. First, charged tracks ionize the argon. The remaining ions produce prompt scintillation light and the corresponding electrons begin to drift towards the wires due to the presence of the electric field. When the drift electrons reach the wire planes a 2D image is produced for each plane. When combining the 2D images from multiple planes along with the scintillation light information a 3D reconstruction is possible.

The general principle of a LArTPC involves utilizing two properties of LAr, scintillation

394 light and ionization. Charged particles travel through the argon and produce scintillation
395 light which is collected by photomultiplier tubes (PMT's). A uniform electric field is applied
396 over active volume which transports the ionization electrons to a series of wire planes.
397 Assuming the argon is pure and has minimal electro-negative contaminants, the wire planes
398 then measure the induced or collected charge signal from the drifting electrons. The planes
399 are each oriented at a different pitch angles. Each plane then can then produce a two
400 dimensional image of the event as a function of wire and time. Combining multiple planes
401 along with the PMT information allows for the object to be fully reconstructed in three
402 dimensions. A diagram of the TPC concept is show in Figure 3.1. In the following sections
403 the TPC, light collection system, and electronics are described in detail.

404 **3.3 Time Projection Chamber**

405 The TPC is the core of the MicroBooNE detector and forms a rectangular prism with
406 dimensions $2.3m \times 2.6m \times 10.4m$ which contains 87t of LAr. The longest dimension, which
407 in MicroBooNE's coordinate system is refereed to as the z-direction, is oriented on axis
408 of the BNB. The majority of the TPC materials are composed of 304V stainless steel
409 and G10. Stainless steel was chosen due to it's low magnetic susceptibility, resistance to
410 corrosion/oxidation, and ability to maintain it's strength in cryogenic temperatures. G10
411 was chosen due to it's ability to perform well as an insulator in cryogenic environments.



Figure 3.2: The MicroBooNE TPC is shown here. On the far right is the flat cathode plane. The far left shows the 8,456 anode wires installed. The field cage tubes, which provide the uniform electric field, span the length between the anode and cathode.

412 The TPC field cage, which provides the uniform electric field through the detector
 413 volume, and was designed to produce field strengths up to 500 v/cm in liquid argon. The
 414 field cage consists of a total of 64 stainless steel rectangular loops that are supported and
 415 evenly spaced by a G10 holder. The cathode plane is a series flat stainless steel sheets that
 416 is opposite the anode sense wires. Figure 3.2 shows the MicroBooNE TPC.

417 Every piece that was used in the MicroBooNE detector was thoroughly cleaned. Many
 418 pieces were cleaned in an ultrasonic cleansing bath while others were cleaned by hand.
 419 The detector was constructed in a clean environment that maintained positive pressure to
 420 mitigate the accumulation of dust. A complete description of the process is summarize in
 421 a separate technical note. []

422 MicroBooNE has a total of 8,265 sense wires that form 3 unique wire planes, one vertical
 423 collection plane (Y) and two induction planes (U,V) oriented at ± 60 relative the Y plane.
 424 The wire planes are separated by 3 mm. The wires in each plane are evenly spaced by 3
 425 mm pitch on carrier boards. The Y plane consists of 3,456 wires with a total of 108 carrier
 426 boards that accommodate 32 wires each. Each of the U and V planes consist of 2,400 wires
 427 with a total of 150 carrier boards that accommodate 16 wires each. The wires themselves
 428 are made of 304V stainless steel and are $150 \pm 5\mu\text{m}$ in diameter. A $2\mu\text{m}$ layer of copper
 429 is plated over the wires to decrease the resistivity from $40\Omega/\text{m}$ to $3\Omega/\text{m}$. The reduced

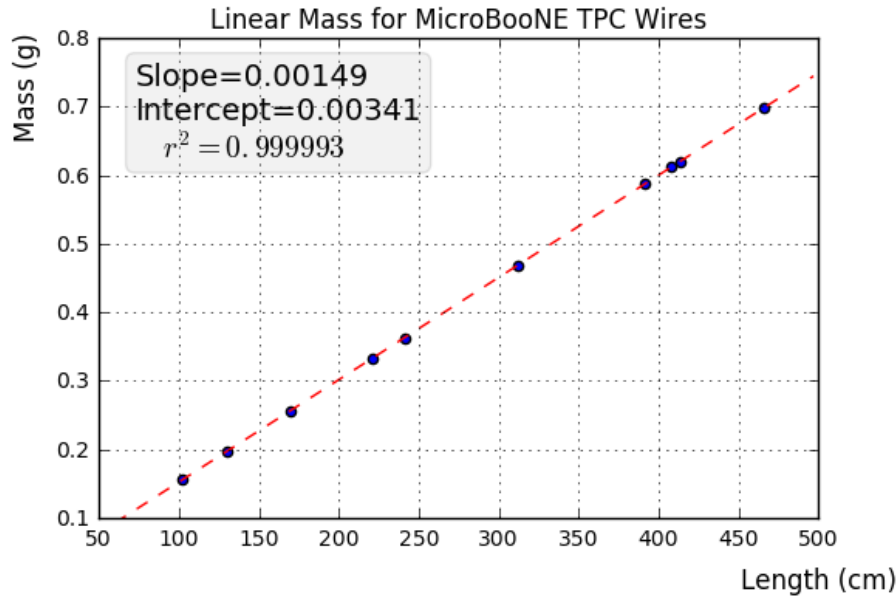


Figure 3.3: This plot is for a small sample used to cross check the linear mass density measured from the wire dealer. The slope from this plot represents the linear mass density and was found to be consistent with the value 0.149g/m

430 resistivity aids in noise reduction at cryogen temperatures. Finally the wire is covered in
 431 and outer layer 0.1 μ m of gold to prevent the copper from oxidizing over time. The linear
 432 mass density of a small sample of wires was measured and is shown in figure 3.3.

433 The wires were designed to installed at a nominal tension of 6.97 N. To account for this,
 434 the carrier boards were installed onto a series of tensioning bars on the anode frame. These
 435 tensioning system, as shown in figure 3.4, allowed for fine tune adjustments to be made to
 436 separate sections of wires.

437 There are a total of 12 tensioning bars, 2 sets of 5 that traverse the entire top and bottom
 438 length of the anode frame, and 2 spanning the entire height of the upstream and downstream
 439 sections of the anode frame. Bronze jacking screws were used for final adjustments once
 440 all the wires were installed. Bronze was chosen since it has a similar thermal expansion
 441 coefficient to stainless steel and it is a softer metal which helps mitigate the risk of cold
 442 welding with stainless steel during the tensioning process.

443 In preparation for installing the actual detector wires, an installation team was trained

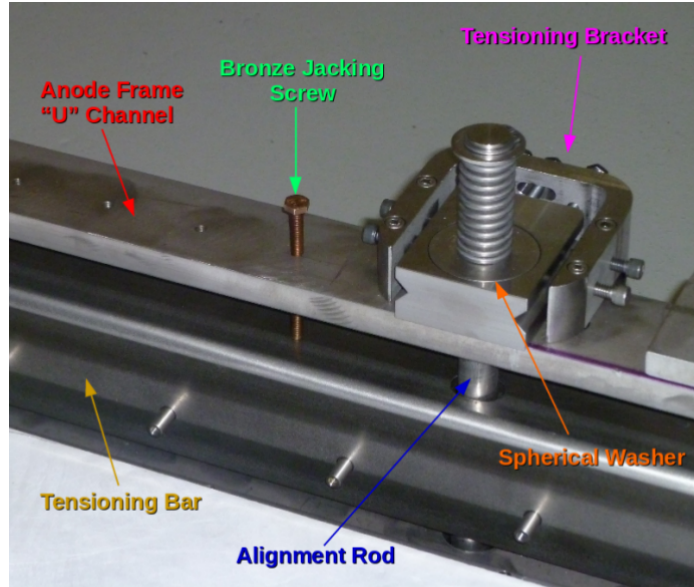


Figure 3.4: The MicroBooNE tension system. Wire carrier boards (not shown here) are mounted on the tensioning bar. The tensioning bar is able to move the wires during the tensioning process. Bronze jacking screws were used for final alignment during the tensioning process

444 on how to properly handle and install them. A 'mock-wire' installation was done to practice
 445 and identify the risks. After this, the actual wires were installed. The installation took
 446 approximately one week. The wires were installed serially, first the Y-plane, then the U-
 447 plane, and then the V-plane. After all the wires were install, a G10 cover board was placed
 448 over carrier boards to secure and protect the electronics on the board, as shown in figure
 449 3.5.

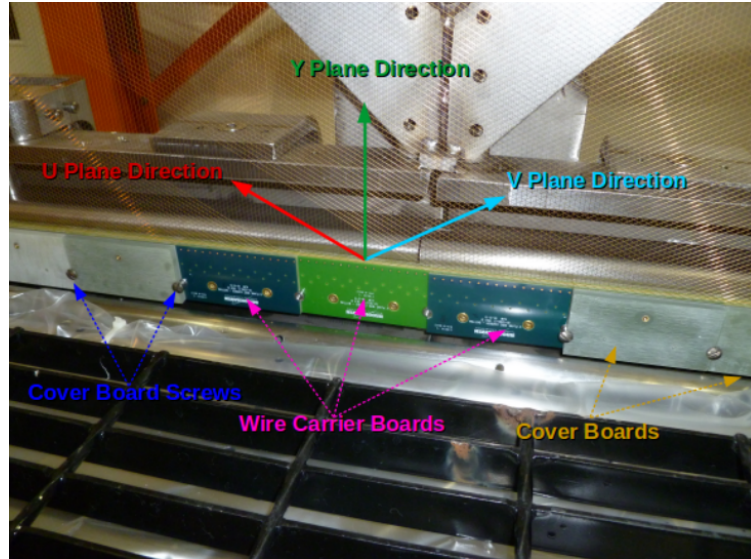


Figure 3.5: The MicroBooNE wires for 3 planes are shown here. The wire carrier boards are serially installed on the tensioning bar. The boards are held in place with a G10 cover plate that is secured with a smooth stainless steel screw.

450 Next, the wires were brought as close to nominal tension as possible. It was decided to
 451 favor under tensioning wires to minimize the risk of a broken wire during the tensioning
 452 process. The wire tensioning was done in a systematic way using the bronze jacking screws.

$$f = \frac{1}{2L} \sqrt{\frac{T}{\rho}} \quad (3.1)$$

453 Each wire has a characteristic resonance frequency that is related to its length, tension,
 454 and linear mass density through equation 3.1. A custom device was made to measure
 455 the resonant frequency of individual MicroBooNE wires. A laser light was focused on a
 456 particular wire and the wire gently plucked. A photo-diode mounted in an optical lens then
 457 measured the intensity of reflected light as the wire vibrated. The signals were then read into
 458 SpectrumAnalyzer, which is a software package that records frequency. SpectrumAnalyzer
 459 also allowed the high order frequency harmonics to be seen. The higher frequencies allowed
 460 for more precise tension measurement as see in Figure 3.6

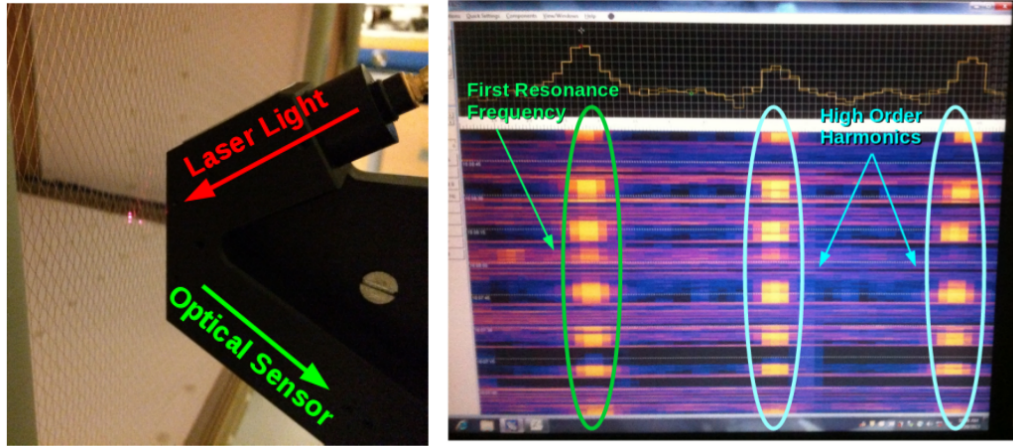


Figure 3.6: Left: Picture of the tension measuring apparatus including a laser and a optical sensor made of a photo-diode and a lens. Right: Example output of the SpectrumAnalyzer showing the first resonance frequency (bright line on the left) and the higher order harmonics (lines in the middle and left).

461 Note that the tension of 2328 out of 2400 U wires, 2308 out of 2400 V wires, and 3410
 462 out of 3456 Y wires was measured, corresponding to 97.5 % of all wires installed in the
 463 detector. Only the wires inaccessible to the tension measuring device were not measured.
 464 The average tension for U,V,Y planes respectively was 0.589 ± 0.012 kg, 0.664 ± 0.014 kg,
 465 0.525 ± 0.009 kg. The tension for each plane is shown in Figure 3.7 and Figure 3.8.

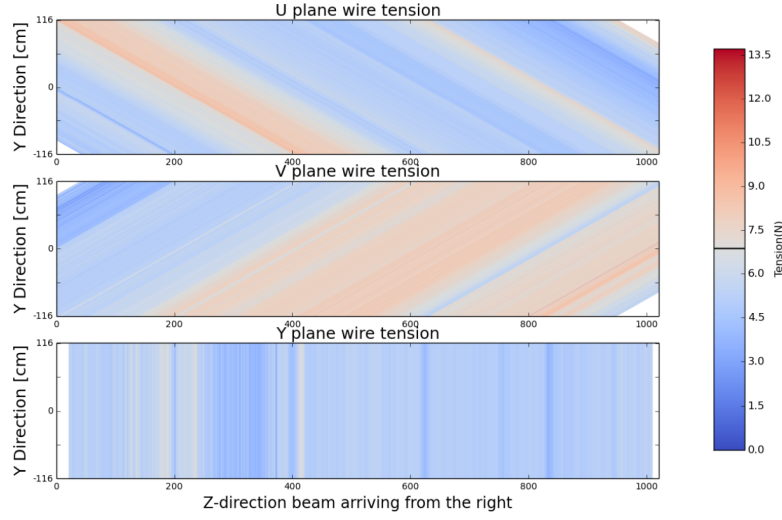


Figure 3.7: This a plane by plane map of the measured wire tensions for MicroBooNE.

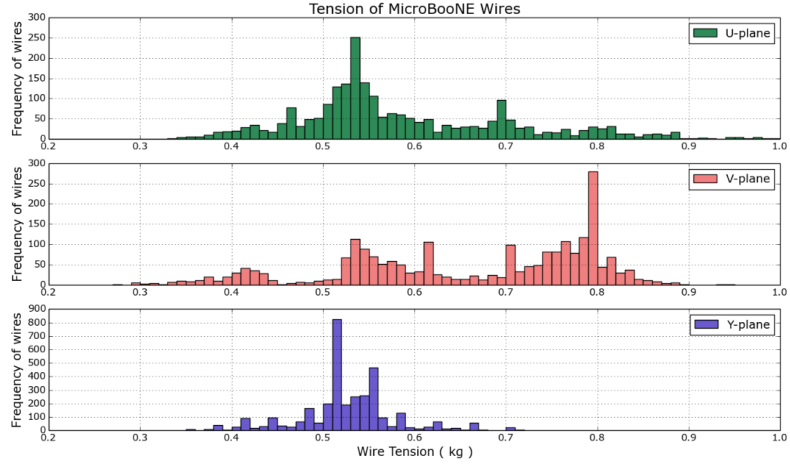


Figure 3.8: This a plane by plane histogram of the measured wire tensions for MicroBooNE.

3.4 Light Collection

The TPC can reconstruct 3D objects but there is still an ambiguity in the initial drift position. The light collection system in an LArTPC provides information to address this degeneracy. Scintillation light of liquid argon is 128nm wavelength and is produced through two primary reactions. The first, which accounts for $\approx 25\%$ of the light yield, is done through a Σ singlet excimer excitation and has a reaction time of 6 ± 2 ns. This type of

472 excimer is formed from an ionized argon atom that combines with another stable argon
 473 atom. The second, which accounts for the other 75% of light yield, is done through a Σ
 474 triplet excimer excitation and has a reaction time of $1590 \pm 100 \mu\text{s}$. The triplet state excimer
 475 is formed from a stable argon atom, an ionized argon atom, and a free electron.^[1] Since the
 476 prompt scintillation light is orders of magnitude faster than drift time from the TPC signal
 477 this information can be used to address this ambiguity.

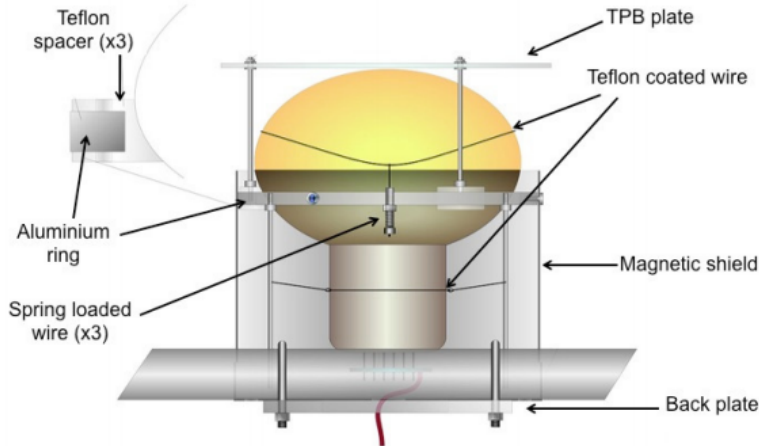


Figure 3.9: Schematic of a PMT optical unit for MicroBooNE.

478 The MicroBooNE light collection system consists of 32 8-inch diameter Hamamatsu
 479 R5912-02mod cryogenic PMTs. The PMT's are not optimized to detect 128nm vuv light.
 480 Therefore, an acrylic plate coated with tetraphenyl butadiene(TPB)^[2] was installed in front
 481 of the PMT's to act as a wavelength shifter. The TPB plate absorbs the 128nm light and
 482 re-emits it a peak wavelength of 425nm. Also, it is known that PMT response is reduced
 483 from certain orientations in the earth magnetic field. To address this a mu-metal shield was
 484 designed to extend just past the equator of the PMTs. A schematic of a PMT optical unit
 485 is shown in figure 3.9.

486 The PMT system is mounted on a railing behind the wire planes and spans the entire
 487 detector length as shown in figure 3.10. This also provides a weak handle on interaction
 488 position since the scintillation light is fairly localized. Most importantly, since MicroBooNE
 489 is a surface detector and constantly being bombarded by cosmic rays, the scintillation flash

490 is used as a method of identifying neutrino interactions coming in time with the beam.



Figure 3.10: PMT optical units installed on support racks inside the MicroBooNE cryostat

491 3.5 Electronics Readout

492 The TPC and PMT systems produce detector analog signals which need to be digitized,
493 transferred out of the detector, and written to disk through data acquisition(DAQ) software.
494 Both systems perform a first round of shaping and amplification in the cold LAr and then
495 interface with warm electronics for further processing. The DAQ continuously writes to disk
496 and creates a buffer which stores data for up to 24 hours. MicroBooNE employs various
497 triggers to signify beam and non-beam data blocks and permanently store data from the
498 buffer stream. A schematic overview of the TPC and PMT signal processing and readout
499 stages is shown in Figure 3.11.

500 For the TPC, a large portion of the electronics processing for the 8,256 wire signals
501 are performed directly in the LAr. To reduce electronics noise, the input distance from
502 the wires to the preamplifier is minimized. The sense wires directly interface with CMOS
503 analog front end ASICs which operate on cold motherboards. In total MicroBooNE has
504 516 CMOS ASICs. The ASICs generate 50 W of heat load which is a negligible impact on
505 the cryogenics system. The motherboards shape and amplify the low noise signal. There

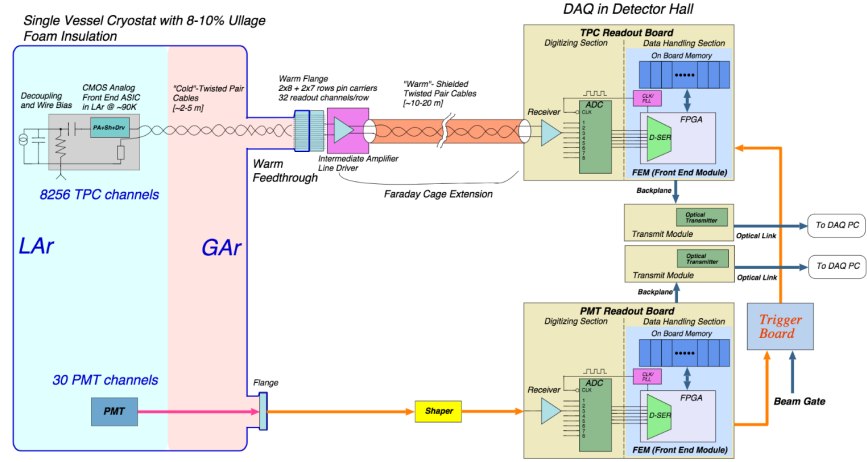


Figure 3.11: MicroBooNE LArTPC and PMT signal processing and readout schematic.

506 are 36 top style motherboards that instrument Y,U and V plane wires and 14 side style
 507 motherboards that instrument U and V plane wires. The signals are then passed through a
 508 series of 12 feedthrough ports to warm electronics. The warm signals are then distributed
 509 over nine readout crates, which digitize the signals.

510 The TPC system read out frame is defined to be 1.6 ms. This number was chosen
 511 to account for ionization electrons that are generated at the cathode and drift the entire
 512 distance to the wires in the presence of a 500V/cm E-Field. In MicroBooNE, an event is
 513 defined as four 1.6 ms readout frames. The additional frames allow for identification of
 514 cosmic particles that arrive before and after the neutrino interaction.

515 The PMT system is also processed in a similar fashion. The PMT's undergo 60 ns
 516 shaping to allow for precise measurements of the signal rising edge. The signals are sampled
 517 at 64MHz but only shaped signals above a threshold are read out and stored for data. The
 518 PMT signals are split into two different gains. A high gain signal that is 10 times the
 519 amplitude of the low gain. The signals are then brought to pre-amp/shaper boards and
 520 digitized and sent to the DAQ.

521 Chapter 4

522 Booster Neutrino Beam

523 Fermilab is one of the world's leading neutrino facilities and currently produces two neutrino
 524 beams that span a wide range of neutrino energies. The Booster Neutrino Beam (BNB),
 525 which will be described in detail throughout this chapter, is a lower energy beam that
 526 delivers neutrinos to various short baseline experiments. Fermilab also hosts the NuMI
 527 (Neutrinos at the Main Injector) Beam [] which produces neutrinos over a large range
 528 between 1GeV/c-30GeV/c and delivers neutrinos to various experiments both on-axis and
 529 off-axis. The NuMI beam will not be covered in this thesis.

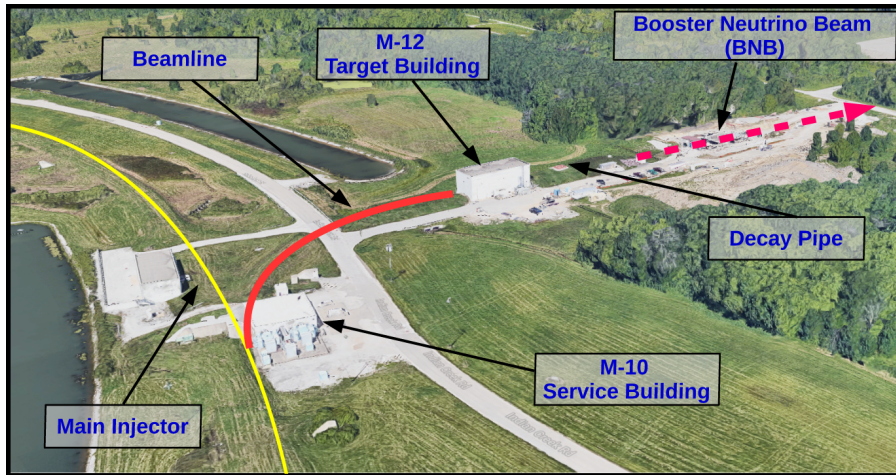


Figure 4.1: This image shows an aerial view of the Booster Neutrino Campus. Protons are extracted before the main injector near the M-10 service building and delivered to the M-12 target hall where the low energy neutrino beam is produced.

530 The Booster neutrino campus is illustrated in figure 4.1. To produce the BNB, protons
531 are extracted from a transfer line just prior to the main injector and then interact
532 with a beryllium target. The following sections will describe the beam system, neutrinoos
533 production process, and flux predictions for the BNB.

534 4.1 Primary Beam, Target and Horn

535 The BNB extracts 8.89 GeV/c momentum protons from the Fermilab Booster synchrotron
536 and delivers them to a beryllium target housed in the M-12 building. The protons from
537 the booster are grouped in 1.6 μ s windows called 'beam spills'. One beam spill contains
538 approximately 5×10^{12} protons. On average the Booster can run no more 5 Hz with no
539 more than 11 pulses in a row at 15 Hz. In optimal running conditions the Booster can
540 deliver 9×10^{16} protons on target (P.O.T) per hour.

541 The beam pipe directly leading to the target is approximately 5 feet long and is held
542 under vacuum to minimize proton interactions not originating from the target. The incom-
543 ing proton flux is measured by a pair of toroids which are positioned upstream of the target
544 and provide an error on P.O.T on the order of 2 %.

545 The target consists of 7 cylindrical beryllium slugs that together produce an effective
546 cylinder of 71.1 cm in length and 0.51 cm in radius. The use of multiple slugs gave the
547 beryllium more surface area to allow efficient heat transfer from a simple air cooling system
548 to be sufficient. An exploded view of the BNB target is shown in figure 4.2. As the protons
549 collide with the beryllium, large amounts of secondary and tertiary mesons, such as π^\pm, K^\pm ,
550 are produced . These mesons will later decay into neutrinos and other decay particles.

551 The target is positioned inside of a large toroidal electromagnet called a horn. The horn
552 is made of an aluminum alloy (6061 T6) and is pulsed with 174 kA of current to produces
553 a $1/R$ field where R is the distance from the axis of the horn. Since neutrinos are neutral
554 particles and can not directly be focused by an electric or magnetic force. Instead, the horn
555 focuses the proper sign parent π^\pm, K^\pm in such a configuration that the neutrino angle from
556 the parent decay particles are focused in a beam.

557 Directly downstream of the horn/target assembly is a collimator that is used to reduced

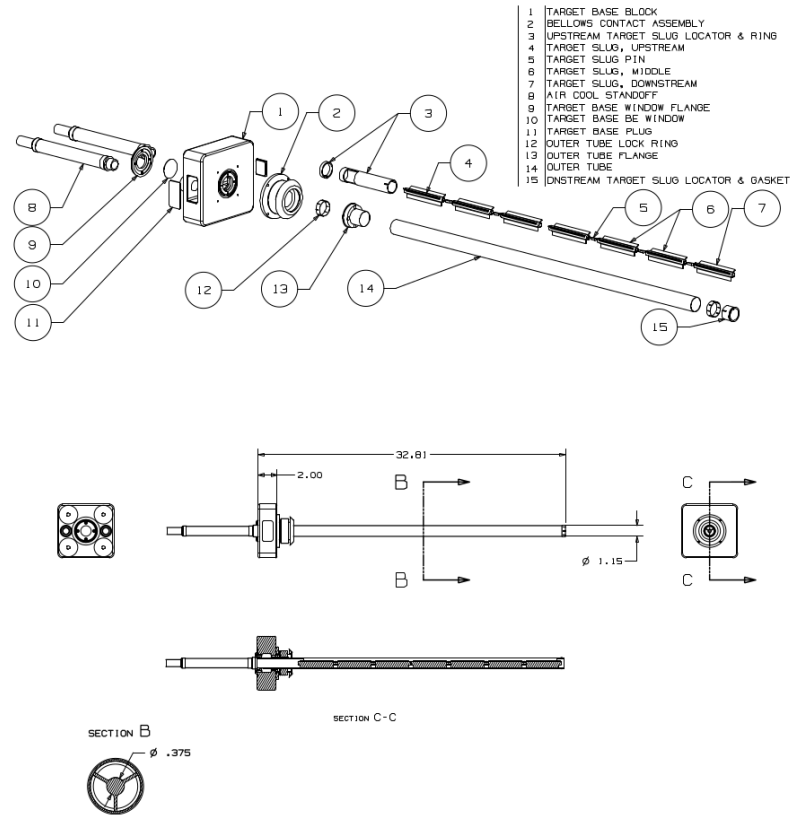


Figure 4.2: An exploded view of the BNB target which shows the 7 Beryllium slugs housed inside the support structure.

background coming from unwanted particles. Particles passing through the collimator enter a 45 m long decay region. In this region, most of the particles decay to produce the neutrino beam. At the end of the decay region there is a beam stop made of steel, concrete. There is also an array of gas proportional counters to detect high energy muons that punch through the beam stop. A diagram of the entire BNB system is shown in figure 4.3. When the horn polarity focuses (negative) positive charged mesons a (anti)neutrino beam is produced.

4.2 Neutrino Flux Prediction

The neutrino flux prediction for MicroBooNE uses the same GENIE simulation files used by MiniBooNE. The files are feed into a Geant4 module that simulates the particles as they

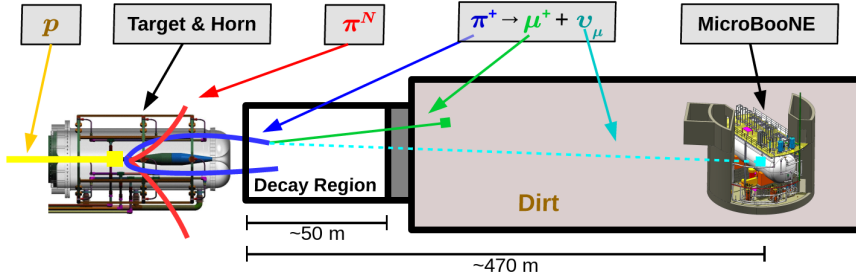


Figure 4.3: This figure shows the Booster Neutrino Beam line at FNAL. The neutrinos are produced in the decay region and then travel towards the MicroBooNE detector located 470 m down stream.

567 travel through the target, horn, and decay region. This produces a MC flux estimate for each
 568 of the various neutrino types. A systematics study was then performed to provide an error
 569 estimate for each of the ν_e , $\bar{\nu}_e$, ν_μ , and $\bar{\nu}_\mu$ flux predictions. To do this, 6 primary systematics
 570 were varied: the production rates of π^+ , π^- , K^+ , K^- , and K_L^0 , and a group systematic
 571 comprised of the horn current miscalibration, skin depth, nucleon inelastic, nucleon QE,
 572 nucleon total cross sections, pion inelastic, pion QE, and pion total cross sections. Beam
 573 errors for each of systematics are shown in Table 4.1 .The final flux estimate with the error
 574 uncertainty is shown in Figure 4.4.

	ν_μ	$\bar{\nu}_\mu$	ν_e	$\bar{\nu}_e$
Delivered P.O.T.	2.00%	2.00%	2.00%	2.00%
π^+	5.8%	0.46%	4.62%	2.66%
π^-	0.01%	7.51%	0.28%	3.20%
K^+	0.38%	0.13%	5.19%	2.61%
K^-	0.01%	0.35%	0.28%	3.92%
K_l^0	0.03%	0.27%	2.36%	22.59%
Other	5.78%	6.09%	3.6%	7.61%

Table 4.1: Systematic errors for production of various neutrino types with respect to their, P.O.T. , parent particle, and other variables.

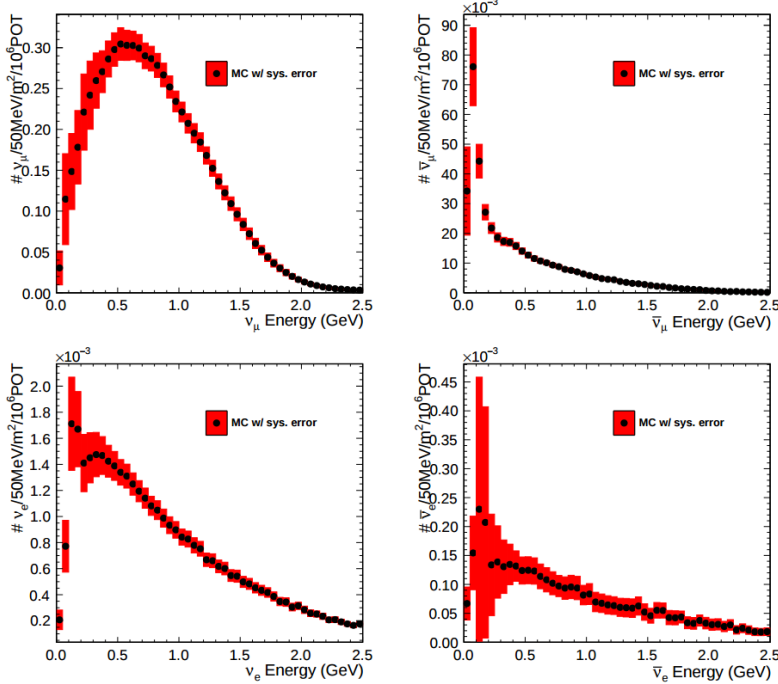


Figure 4.4: Monte Carlo flux predictions for the BNB neutrino spectrum. The red band represents the flux systematic errors. Note the orders of magnitude with the ν_μ spectrum rates.

575 Chapter 5

576 Low Energy Excess and Relevant 577 Cross Sections

578 5.1 Overview

579 This chapter will discuss various facets of what is commonly called the “MiniBooNE Low
 580 Energy Excess.” First, we will present the anti-neutrino excess observed by LSND and how
 581 the oscillation results can be interpreted. Then, we will discuss the efforts of MiniBooNE to
 582 understand the LSND results along with their oscillation results that establish the “Mini-
 583 BooNE Low Energy Excess.” We will also discuss the neutral current $1\pi^0$ cross section
 584 which is the dominant background in the oscillation analysis claims for both MiniBooNE
 585 and LSND. Finally, we will discuss MicroBooNE’s role towards addressing understanding
 586 the low energy excess claims of MiniBooNE.

587 5.2 LSND Excess

588 The Liquid Scintillator Neutrino Detector (LSND) was a 167 ton neutrino detector stationed
 589 at Los Alamos National Lab (LANL) designed to study neutrino oscillations. The detector,
 590 which hosted 1220 PMT’s for event detection, was place 30 m away from the source of a
 591 low energy (40 MeV) $\bar{\nu}_\mu$ beam. Using the Los Alamos LAMPF beam, 800 MeV protons
 592 interacted with a water target to produce π^+ mesons which decayed into $\mu^+ + \nu_\mu$. The μ^+

593 would then interact with a copper beam stop and decay at rest to produce the low energy
 594 $\bar{\nu}_\mu$ beam.

595 The detector medium was primarily carbon (mineral oil CH_2). LSND could easily
 596 distinguish between electromagnetic showers (electrons/positrons/photon) or tracks (pi-
 597 ons/muons/protons) by differences in the Cherenkov cone that was produced. The oscil-
 598 lation signal interaction was $p + \bar{\nu}_e \rightarrow n + e^+$. The primary e^+ is easily visible from the
 599 Cherenkov light it produced but a neutron will not produce Cherenkov light and therefore
 600 be invisible to the detector. The organic scintillator b-PDB was dissolved to the mineral
 601 oil at a concentration of 31 mg/l. The scintillator allowed the 2.2 MeV photon from the
 602 capture of the neutron on hydrogen to be detected. This allowed LSND a unique signal to
 603 identify $\bar{\nu}_e$ interactions. It should be noted that the detector technology could not easily
 604 discriminate between photons, electrons or positrons induced electromagnetic showers.

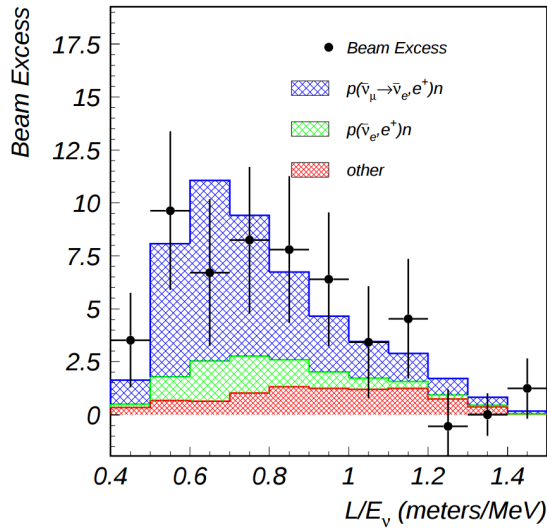


Figure 5.1: This is the LSND neutrino oscillation appearance plot as a function of L/E and represents the 87 event $\bar{\nu}_e$ excess claimed by the experiment.

605 In 2001, the collaboration published results for an observed excess of $87^{+22.4}_{-6.0}$ events
 606 above the predicted background as shown in figure 5.1. If the excess is interpreted as
 607 neutrino oscillations from a two neutrino model, the best fit of the excess would suggest a
 608 $\sin^2(2\theta) = 0.003$ and $\Delta m^2 = 1.2\text{eV}^2$ which greatly contradicts many other measurements
 609 for $\Delta m_{2,3}^2$ or $\Delta m_{1,3}^2$ [1]. One explanation for the excess suggests the idea of mixing between
 610 other additional neutrino states. These neutrinos are called ‘sterile’ since they cannot
 611 directly couple via weak interaction as mentioned prior from the constraints from LEP.

612 5.3 Miniboone Excess

613 The Mini Booster Neutrino Experiment(MiniBooNE) was designed to address the claims of
 614 the LSND $\bar{\nu}_e$ excess result. The MiniBooNE detector was a mineral oil Cerenkov detector
 615 designed to be a similar technology to LSND. MiniBooNE, stationed at FNAL in the BNB,
 616 was positioned 541 m from the neutrino source and was able to receive both ν_μ and $\bar{\nu}_\mu$
 617 fluxes. The distance was chosen such that the L/E parameter were similar to that of the
 618 LSND experiment.

619 MiniBooNE, which contained 818 tons of mineral oil(CH_4), was located underneath
 620 more than 3m of earth overburden to help reduce cosmic rays. The detector supported a 35
 621 cm thick outer cosmic veto using 240 PMT’s. The veto efficiency was 99.99% for rejecting
 622 cosmic muons. The inside of the detector was instrumented with 1,280 8-inch PMT’s
 623 which were used to read out neutrino and comsic data. Cherenkov light from different
 624 particles produced distinct patterns on various PMT’s inside the spherical detector. A
 625 cartoon showing various type of signal topologies from the MiniBooNE detector are shown
 626 in figure 5.2. The detector energy scale was calibrated in situ by fitting various parameters
 627 from thoroughgoing muons, decay Michele electrons, and π^0 decays’s. A clear limitation of
 628 Cherenkov detectors is the inability to concretely distinguish between photon induced or
 629 electron induced showers.

630 The primary oscillation analysis for MiniBooNE was done ‘blind’ in an attempt to
 631 gain confidence from the physics community upon it’s findings. The entire analysis was
 632 developed on large statistics Monte Carlo simulation and a small sample of test data. In

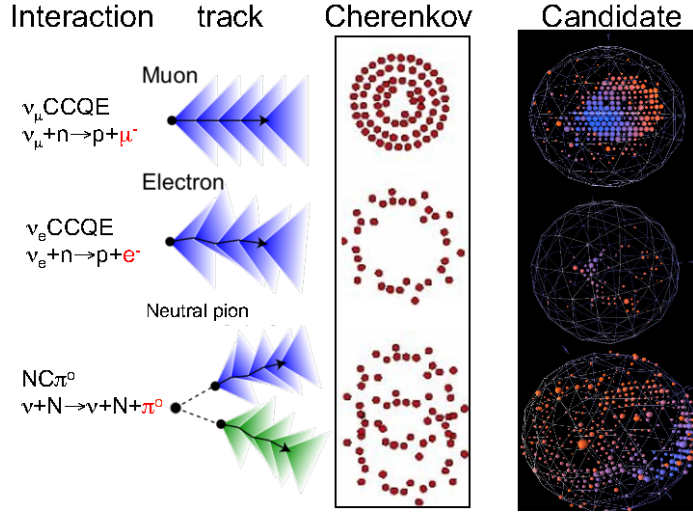


Figure 5.2: This cartoon depicts different particle interactions as observed in Cherenkov detector. The far right shows the interaction types as viewed in MiniBooNE

total, MiniBooNE accumulated 6.46×10^{20} P.O.T. of ν -data and 11.27×10^{20} P.O.T. of $\bar{\nu}$ -data. Fermilab's ability to support both neutrino and anti-neutrino beams allow for MiniBooNE to confirm that an LSND-like excess was independent of neutrino type. The data is in good agreement between signal and background predictions and contradicts the LSND claim up to 98% confidence in both modes above 500 MeV. The excess is most prominent in the region of events below 500 MeV, as seen in figure 5.3. In this region the largest background comes from π^0 -misidentification followed by photons coming from radiative Delta decays. MiniBooNE reports a total excess of 240.0 ± 62.9 combine $(162.0 \pm 47.8\nu, 78.4 \pm 28.5\bar{\nu})$ events in the neutrino energy range $200 < E_\nu^{QE} < 1250$ MeV. Also, if the excess is interpreted as a two flavor oscillation the inferred parameters are consistent with the LSND result.

5.4 Neutral Current π^0 production

The leading background from the MiniBooNE oscillation result, as mentioned in chapter 5.3, is π^0 -misidentification. Accurately measuring the neutrino induced neutral current single π^0 production cross section is therefore crucial in understanding background contributions for an oscillation analysis. Charge current π^0 production conveniently has an outgoing

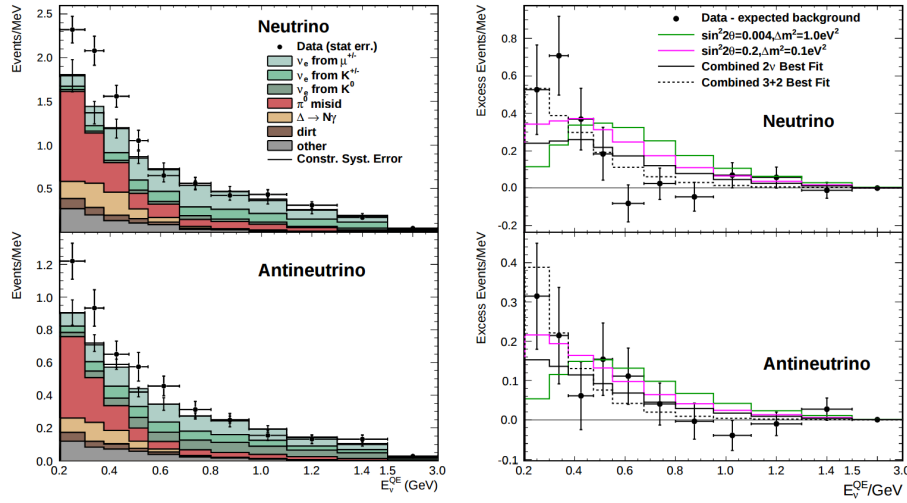


Figure 5.3: The left plots show the stacked histograms for signal and background overlaid with data for both neutrino and anti-neutrino modes. The right plots show the relative excess as a function of neutrino energy and make obvious the energy range that drives the excess.

648 charged muon in the final state and is very easy to identify. On the other hand, neutral
 649 current π^0 production does not guarantee any outgoing charged particles and therefore,
 650 makes identification much harder. For neutrinos in the BNB, the main production mode
 651 for neutrino induced neutral current π^0 production is via the $\Delta(1232)$ resonant production.
 652 Resonant production is when a baryon, such as a proton or neutron, are excited to a higher
 653 resonance state and then subsequently decays back to the initial state while liberating a
 654 π^0 . There are other neutrino induced π^0 production modes that MicroBooNE is sensitive to
 655 such as deep inelastic scattering and coherent production, but have a lower production cross
 656 section at the given BNB neutrino energy range. A general Feynman diagram can be used to
 657 describe the main components of neutrino induced neutral current single π^0 production in
 658 argon as seen in Figure 5.4.

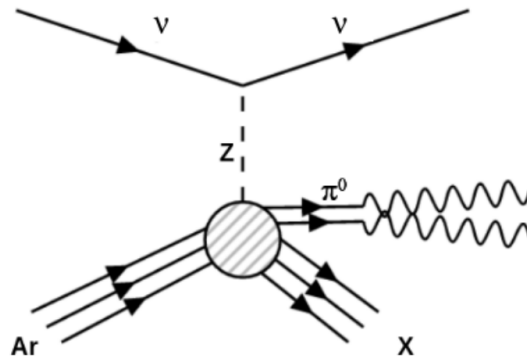


Figure 5.4: Neutrino induced single π^0 production on argon. This topology is defined such that 1 π^0 is produced and the other particles leaving the interaction (X) must only consist of nucleons.

⁶⁵⁹ 5.5 NC-Pi0 in Carbon vs Argon

⁶⁶⁰ In 2010, MiniBooNE measured the total neutral current single π^0 cross section on carbon
⁶⁶¹ with what is currently the worlds largest statistics sample of π^0 s. The MiniBooNE neutral
⁶⁶² current single π^0 signal is defined as a topology that produces one and only 1 π^0 in the
⁶⁶³ final state with no other other charged leptons or mesons originating from the vertex. In
⁶⁶⁴ 2015, the first measurement of neutrino induced neutral current π^0 production on argon was
⁶⁶⁵ measured by ArgoNeut collaboration at Fermilab while running in the NuMI neutrino beam.
⁶⁶⁶ ArgoNeut, being a smaller detector, could not easily contain many of the electromagnetic
⁶⁶⁷ showers from π^0 decays. This forced the analysis choose a slightly different final state signal
⁶⁶⁸ definition requiring there to be at least one π^0 , no electron or muon, and allowing there
⁶⁶⁹ to be any number of mesons in the final state. This modified signal definition makes any
⁶⁷⁰ comparison to other historical data very complicated.

⁶⁷¹ MicroBooNE, which resides in the same neutrino beam line as MiniBooNE, is a prime
⁶⁷² candidate for various studies of neutral current π^0 production studies between different
⁶⁷³ target materials(C/Ar). Being a larger LArTPC, more π^0 decays will be contained allowing
⁶⁷⁴ for high statistics measurements of the cross section along with the general need to measure
⁶⁷⁵ the production rate as input to its own oscillation analysis.

676 Chapter 6

677 Cosmogenic π^0 's at MicroBooNE

678 In this chapter we will talk about some of the challenges and interesting physics cases re-
679 garding cosmogenics in a surface LArTPC. Many cosmic ray particles penetrate surface
680 detectors and populate the detector region making it necessary to remove these particles
681 from reconstruction and address charge contamination in neutrino events. The majority
682 of this chapter will emphasize cosmogenic track removal, electromagnetic showers and sub-
683 sequently π^0 selection. We will first examine some historical cosmogenic studies from the
684 Icarus experiment. Then, introduce what MicroBooNE can contribute in terms of under-
685 standing cosmics. We will address the cosmic simulation that is used, various steps in
686 reconstruction and pattern recognition used to select π^0 's in a LArTPC. Finally, we will
687 conclude with how these studies impact future cross section analyses and backgrounds to-
688 ward the low energy excess analysis.

689 6.1 Motivation

690 Cosmogenic particles allow for the separate test of reconstruction tools along with an inde-
691 pendent way to address the detector energy scale. The high rate of surface cosmics cause
692 some trouble with disentangling signal neutrino events so cosmic ray removal. Luckily, off
693 beam surface cosmogenic samples allow for a large statistics dataset to develop and optimize
694 reconstruction techniques. Cosmogenic muons that traverse the detector provide a handle to
695 understand detector energy scale along with understanding track reconstruction efficiency.

696 Stopping muons that produce a Michele electron help provide a benchmark for low energy
 697 showers in the 10's of MeV range. The π^0 resonance, with a mass of $134.9 \text{ MeV}/c^2$, can be
 698 used as a standard candle to benchmark overall detector energy scale. The calculate the π^0
 699 mass, as shown in equation 6.1, depends on a measurement of energy and photon opening
 700 angle.

$$\mathcal{M} = \sqrt{2E_1E_2(1 - \cos\theta_{12})} \quad (6.1)$$

701 Electromagnetic shower reconstruction for LArTPC's is well known to be a hard task.
 702 The high resolution of the 2-dimensional projections of EM-showers introduce many chal-
 703 lenges to develop unbiased and fully automated reconstruction. In 2001, the T600 ICARUS
 704 detector ?? performed a surface test run in Pavia, Italy. During this 100 day test the detec-
 705 tor collected over 30,000 cosmic ray events. In 2008, the ICARUS collaboration published
 706 a study of electromagnetic showers coming from π^0 decays in the Pavia dataset. To select
 707 candidate π^0 events, ICARUS hand scanned a total of 7,500 potential events from a PMT
 708 triggered sample. Their hand scanning requirements included, that at least two well sep-
 709 arated electromagnetic showers were visible, a valid t_0 time for the vertex, and that there
 710 was not much charge contamination coming from a nearby cosmic muon. After this, they
 711 were left with 212 hadronic interactions with at least one candidate neutral meson' which
 712 they then proceeded to reconstruct. Their final reconstruction consisted of energy scaling
 713 to account for missing charge in the shower and a minimization against the true π^0 mass
 714 (134.9). An example of one of their hand scanned clustering events is shown in Figure 6.1.

715 MicroBooNE, being a surface detector, is in a position to do a similar study with im-
 716 proved reconstruction techniques. Also, understanding the cosmic production rate for single
 717 π^0 's is valuable to any MicroBooNE analysis that involves EM-showers. The following sec-
 718 tions will present MicroBooNE's Monte Carlo simulation and state of the art reconstruc-
 719 tion techniques.

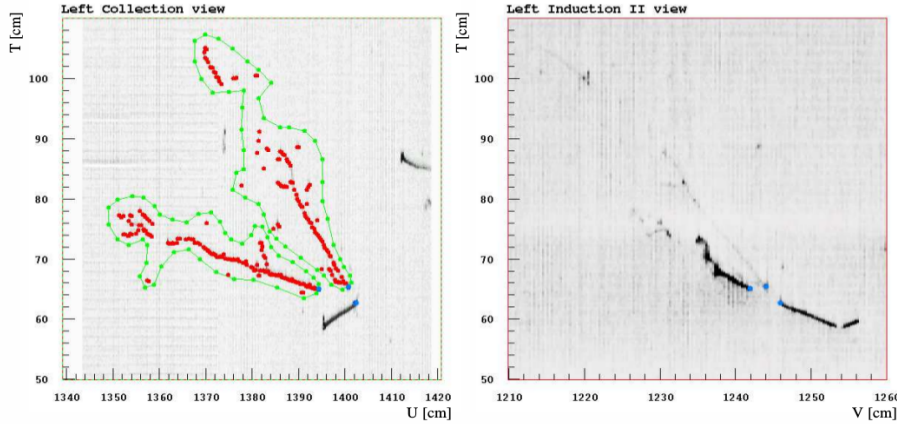


Figure 6.1: A cosmic π^0 from the ICARUS Pavia run. The left image, shows the hand drawn clustering and positions of the shower conversion point and vertex point. The right image, shows the same event on a different wire plane view.

6.2 Traditional Reconstruction

The traditional approach for LArTPC reconstruction involves grouping drift charge that is deposited on the wires to form wire-hits. The light collection system also has light-hits which corresponded to collected light of an individual track or shower. A group of PMT's that have light-hits at the same time is called a flash. Hits from each of the wire planes are clustered together with various reconstruction algorithms to form reconstruction objects that relate to individual particles in the detector. There are two primary reconstruction objects: tracks, which are mostly linear and compact clusters that represent muons, protons, and charged pions, and showers which are more fuzzy shaped cluster objects that represent photons and electrons. Next, to reconstruction a 3D object, an algorithm must match the same 2D cluster objects in at least two of the three wire planes. For MicroBooNE, and the general LArTPC community, matching track reconstruction is well advance but shower reconstruction suffers many hurdles. In recent years lots of progress has been made for LArTPC shower reconstruction. Various different techniques such as: improved 2D clustering and matching techniques[], sophisticated pattern recognition tools[] , and deep learning[] approaches have been explored and each has it's various strengths and weaknesses.

⁷³⁶ **6.3 Wire Cell Imaging**

⁷³⁷ The traditional approach is not the only way to reconstruct LArTPC data. Instead, wire
⁷³⁸ data can be treated with a tomographic approach directly producing a set of 3D space
⁷³⁹ points. Although computationally intensive, this approach allows for more information to
⁷⁴⁰ be used in a 3D clustering framework which can directly impact shower reconstruction and
⁷⁴¹ mitigate degeneracies from the 2D matching method.

⁷⁴² The Wire-Cell framework, spearheaded by Brookhaven National Labs (BNL), utilizes
⁷⁴³ this approach to create 3D space points from MicroBooNE's TPC data. The approach
⁷⁴⁴ relies on the assumption that the same amount of ionization charge is seen on each plane.
⁷⁴⁵ In MicroBooNE this is done by reconstructing small time slices on each wire planes. Each
⁷⁴⁶ time slice involves solving a charge equation for all possible hits with respect to the matrix of
⁷⁴⁷ hits actually recorded in the time slice. The charge equation is shown in equation 6.2. The
⁷⁴⁸ detector wire signals are represented in matrix W while all potential wire hits are contained
⁷⁴⁹ in H. Nonzero values in the Q matrix will correspond to unique wire-plane intersections of
⁷⁵⁰ charge, near zero values represent ghost hits due to degeneracies in the charge equation.

$$\begin{bmatrix} W_{u_1} \\ \vdots \\ W_{u_n} \\ W_{v_1} \\ \vdots \\ W_{v_n} \\ W_{y_1} \\ \vdots \\ W_{y_n} \end{bmatrix} = \begin{bmatrix} Q_{u_1}^{H_1} & Q_{u_1}^{H_2} & \dots & \dots & \dots & Q_{u_1}^{H_{m-1}} & Q_{u_1}^{H_m} \\ \vdots & \vdots & \ddots & \ddots & \ddots & \vdots & \vdots \\ Q_{u_n}^{H_1} & Q_{u_n}^{H_2} & \dots & \dots & \dots & Q_{u_n}^{H_{m-1}} & Q_{u_n}^{H_m} \\ Q_{v_1}^{H_1} & Q_{v_1}^{H_2} & \dots & \dots & \dots & Q_{v_1}^{H_{m-1}} & Q_{v_1}^{H_m} \\ \vdots & \vdots & \ddots & \ddots & \ddots & \vdots & \vdots \\ Q_{v_n}^{H_1} & Q_{v_n}^{H_2} & \dots & \dots & \dots & Q_{v_n}^{H_{m-1}} & Q_{v_n}^{H_m} \\ Q_{y_1}^{H_1} & Q_{y_1}^{H_2} & \dots & \dots & \dots & Q_{y_1}^{H_{m-1}} & Q_{y_1}^{H_m} \\ \vdots & \vdots & \ddots & \ddots & \ddots & \vdots & \vdots \\ Q_{y_n}^{H_1} & Q_{y_n}^{H_2} & \dots & \dots & \dots & Q_{y_n}^{H_{m-1}} & Q_{y_n}^{H_m} \end{bmatrix} \begin{bmatrix} H_1 \\ H_2 \\ \vdots \\ H_{m-1} \\ H_m \end{bmatrix} \quad (6.2)$$

751 Then, each ‘slice’ is stacked to it’s corresponding x position. This produces a set of 3D
752 space points that can used in patter recognition algorithms to identify different particles
753 in the data. All reconstruction is done with accounting for known detector dead regions.
754 The current state of MicroBooNE’s signal and noise processing and imaging that requires
755 a minimum of 2 wire planes to be matched from the charge equation.

756 **6.4 Pattern Recognition**

757 Various pattern recognition tools are needed to address MircoBooNE’s TPC data but for
758 this analysis they can be generalized into two efforts, cosmic track removal and EM-shower
759 clustering. Both approaches require different techniques. First, we will focus on optimizing
760 track removal. This involves identifying tracks that are thoroughgoing, and contained. Once
761 all the charge associated with tracks are removed, the remaining charge is clustering into
762 candidate EM-shower objects. Finally, correlated shower pairs are identified and selected
763 as candidate π^0 events.

764 A image of a typical MicroBooNE cosmic event reconstructed with 3D wire cell space
765 points are shown in Figure 6.2 using the BEE viewer []. A detailed list of reconstruction
766 and selection parameters are listed in appendix ??

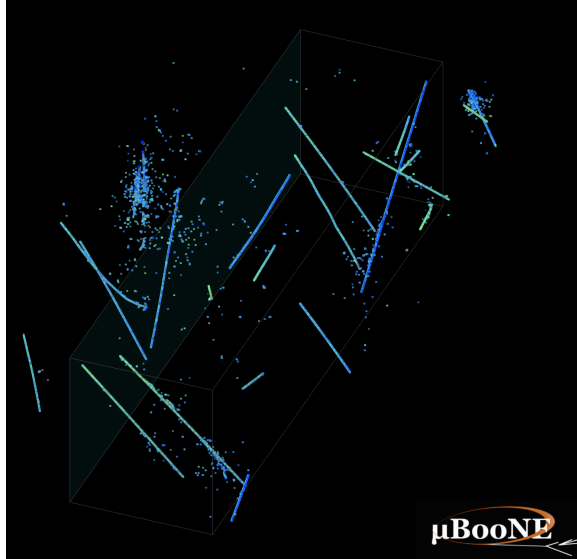
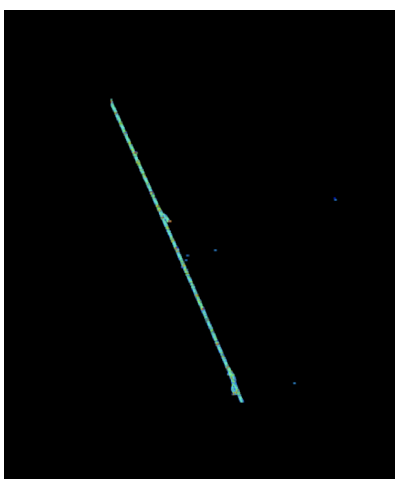


Figure 6.2: This is a typical cosmic event in the MicroBooNE detector. The data used to generate this event is CORSIKA MC.

767 6.4.1 Clustering

768 The wire cell data produces a set of 3D space points as mentioned in section 6.3. Only space
 769 points that are in the fiducial volume are clustered and considered in the reconstruction
 770 process. First a threshold cut of 500 Q is applied to all the remaining space points. This
 771 is done to remove very low charge ghost points and reduce the overall number of points to
 772 cluster. The main goal of this step is to identify the large scale structure of the cosmic
 773 tracks in the data. Additionally, with a smaller number of space points the computational
 774 time for reconstruction is reduced.

775 The first stage of clustering uses BIRCH (balanced iterative reducing and clustering
 776 using hierarchies). The hyper parameters were tuned such that cosmic tracks are removed
 777 with minimal impact to showers involved from π^0 . Birch clustering was chosen because it
 778 scales well with large number of points, efficiently maintains large number of clusters in
 779 datasets and also handles outliers removal well. This clustering technique leverages on
 780 the inherent structure of track like particles having a well defined 3-dimensional trajectory.
 781 Particles such as protons, muons, and charged pions are continuously ionizing meaning
 782 that there should be no gaps in the detected charge. This feature is much different than



(a) This figure shows an image of muon track as viewed from the BEE-WireCell image viewer.



(b) This figure shows an image of $\pi^0 \rightarrow \gamma\gamma$ decay as viewed from the BEE-WireCell image viewer.

783 EM-showers which have lots of gaps between detected charge. An example of this is shown
784 in figure ??

785 The next stage of the track and shower clustering process is to merge together proto-
786 clusters that did not get fully grouped together in the BIRCH clustering step. The second
787 pass clustering is geared toward larger object clustering. To address this, a 3D convex hull
788 is constructed around every cluster. Next, the euclidean distance between all the vertex
789 points calculated. If the minimum merging distance is small, the clusters from tracks get
790 merged together well. Clusters from showers still need further.

791 The final stage of clustering is shower clustering. This requires there to be a distinction
792 between a cluster object that is shower-like or track-like. To do this, parameters that
793 describe various aspects of a cluster are calculated. The most important features from
794 the cluster parameters are cluster length and spread of the first principle component. More
795 details about track and shower selection are described later in section 6.5.

796 Once defined as a shower cluster, a 3D charge weighted axis is fit to the cluster's set
797 of space points. First, a distance of closest approach (DOCA) for each cluster axis pair
798 is calculated and a proto-vertex is calculated at the midpoint of the DOCA line. Next,
799 a unique conversion point is calculate for each shower pair to identify the start point of

800 the shower. This can also be thought of as a proxy for the photons conversion point. Using
 801 the prot-vertex point and two conversion points an opening angle is calculated. A pair of
 802 clusters that have a DOCA that is less than 5 cm, an angle between 15 and 165 degrees,
 803 and both of the conversion lengths are less than 20 cm are merged together. The merging
 804 is done for all shower cluster pairs.

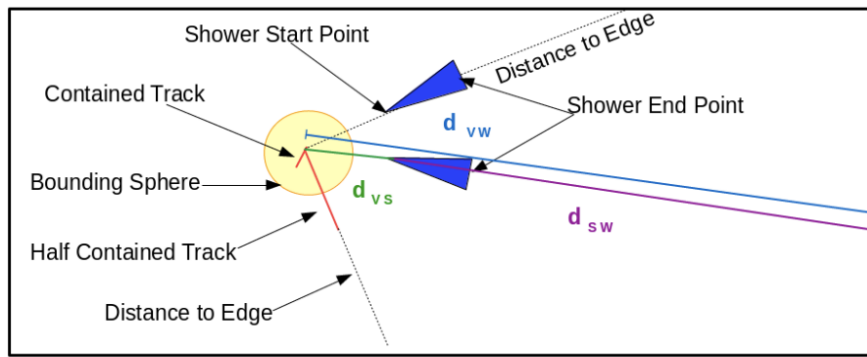


Figure 6.3: This graphic illustrates all the data objects and relevant parameters. The shower objects are shown in blue, track objects shown in red, and a bounding sphere, used to associate tracks with the vertex, is shown in yellow.

805 6.5 Track and Shower Selection

806 6.5.1 Track Removal

807 For this analysis track removal is handled in a unique manner. The primary goal is to
 808 identify showers coming from a π^0 . Therefore, all cuts and optimizations will be teste
 809 d against shower objects. The general approach for track removal depends heavily on
 810 geometric properties such as length and linearity of the cluster.

811 6.5.2 Single π^0 Reconstruction

812 The vast majority(98.8%) of π^0 's decay into two photons. The relationship for the par-
 813 ticle mass, which was defined in eq6.1, shows the importance of properly accounting for
 814 the energy and angle between the decay photons. To understand a baseline for reconstruc-

tion efficiency we have generated a sample of 10,000 single particle π^0 events isotropically throughout the detector volume with initial momenta spanning from 0 to 2 GeV.

First we will investigate energy deposited in detector from the decay. An plot of the true kinematic energy of photons from the decay particle is shown in Figure 6.4. It is important to note that both photons need to be reconstructed to form a resonant mass. This means that we are driven to optimize the reconstruction to be robust around showers in the range of many 10's of MeV in deposited energy. Photons that convert near the fiducial edge of the detector can escape and deposit only a small amount of energy in the detector. This poses problems for capturing the total amount of energy of the shower and drives the need for a fiducial cut around the edges.

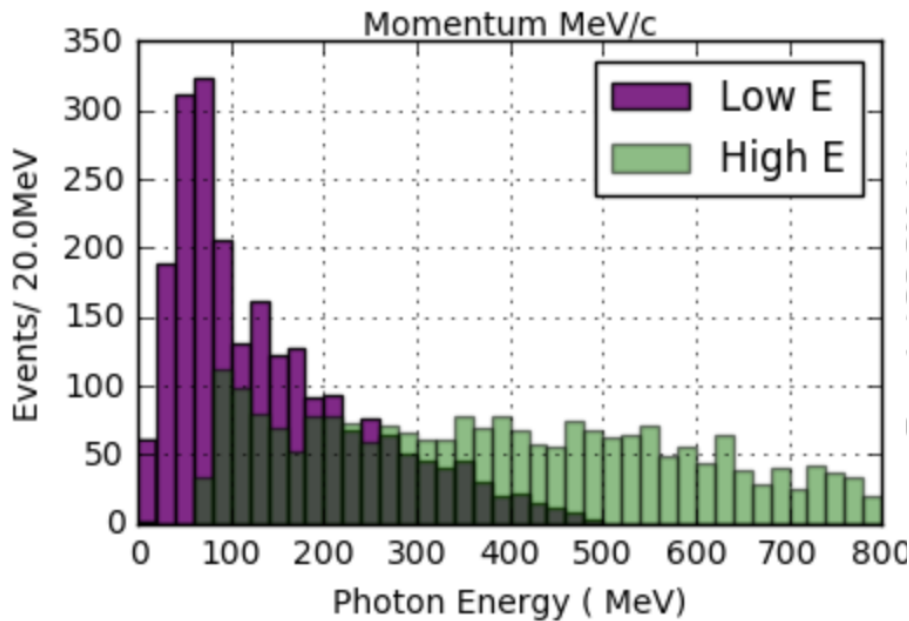
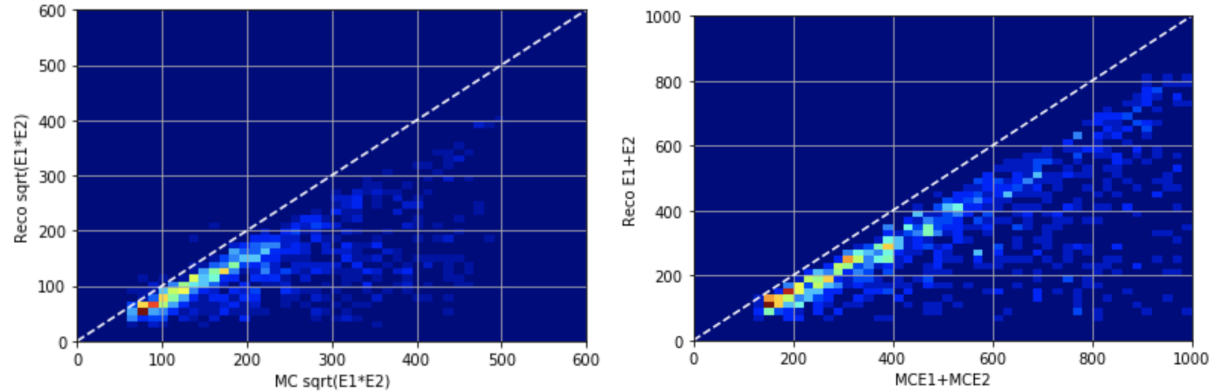


Figure 6.4: This figure shows the photon distribution for π^0 decays from a single particle sample of between 0-2GeV. The higher energy photon is shown above in green along with the corresponding lower energy photon shown in magenta.

To understand the reconstruction accuracy for the energy we are most interested in two metrics. The first is the total collected energy deposited by the two showers. This informs us that we are accounting for most of the energy deposited and handling the fiducial cuts



(a) Scatter plot of reconstructed energy sum vs true energy sum
(b) Scatter plot of reconstructed energy product vs true energy product

Figure 6.5: Reconstructed energy sum and energy product for shower pairs. Both, the reconstructed energy sum and product is less than the true energy deposited.

well. The second is the product of the two shower energies. This directly impacts the reconstructed mass resolution and informs us that we are properly clustering energy between the two showers properly. In figure 6.5 both metrics are plotted for reconstruction against true. Points along the diagonal would represent accurate model predictions. As we will see later in this chapter, the energy product drives the width of the mass resolution.

Next we will investigate the effects of the opening angle between the two photons. The minimum opening angle of the photons is constrained by the momentum boost as the particle decays as shown in equation 6.3. The angular resolution is a very challenging problem in LArTPC's using the traditional 2D projection approach. Fortunately, direct 3D reconstruction improves the angular resolution and allows for a better measurement of shower direction.

$$\sin \frac{1}{2} \theta_{min} = \frac{M}{E_{\pi^0}} \quad (6.3)$$

A plot of the reconstructed vs true opening angle is shown in Figure 6.6. The $1 - \cos\theta$ term from equation 6.1 is sensitive to tails of the mass distribution.

Next, we apply a final set of selection cuts. First, we require that the distance of closest

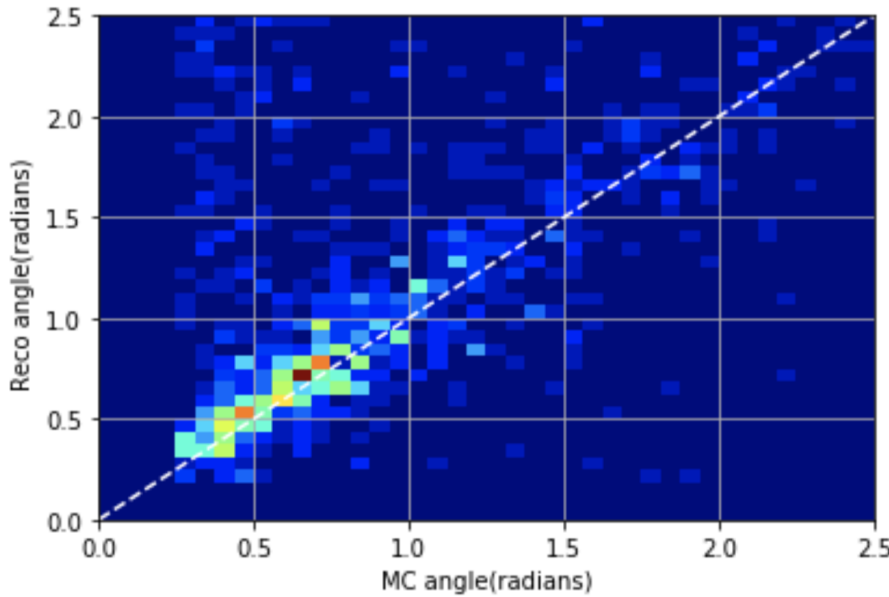


Figure 6.6: This scatter plot shows the reconstructed opening angle vs. true opening angle. We see that the reconstruction does very well with reconstructing this quantity due to the use of wire-cell's 3D approach. When the reconstruction performs badly it tends to identify small opening angles as large ones since we are not using any vertex information.

approach between the two shower axis is less than 5 cm. This is to help ensure that the photons are originating from a common origin. Next, the photon conversion distance can not be longer than 70 cm. This is done to help identify showers that are correlated from the same decay. Finally we only accept showers that are above 50 MeV in reconstructed energy. Figure 6.7 shows the effect of various parameters as applied to the reconstruction. We find that the deficit in mass peak is mainly due to the energy reconstruction. This is due to the missing energy during clustering . For this analysis there is also an additional component of energy missing since we will not be using the initial t_0 -tag. Without using t_0 , there is no effective way to correct back for electron drift effects. Thankfully, this effect is can be captured in understanding the distribution of reconstructed mass peak in the Monte Carlo.

Finally, we address the over all efficiency for reconstruction. The average reconstruction efficiency between 0 and 1 GeV/c is 40.1%. The reconstruction efficiency is shown in Figure 6.8. As can be seen there, the efficiency drops at low and high energies. At low momentum

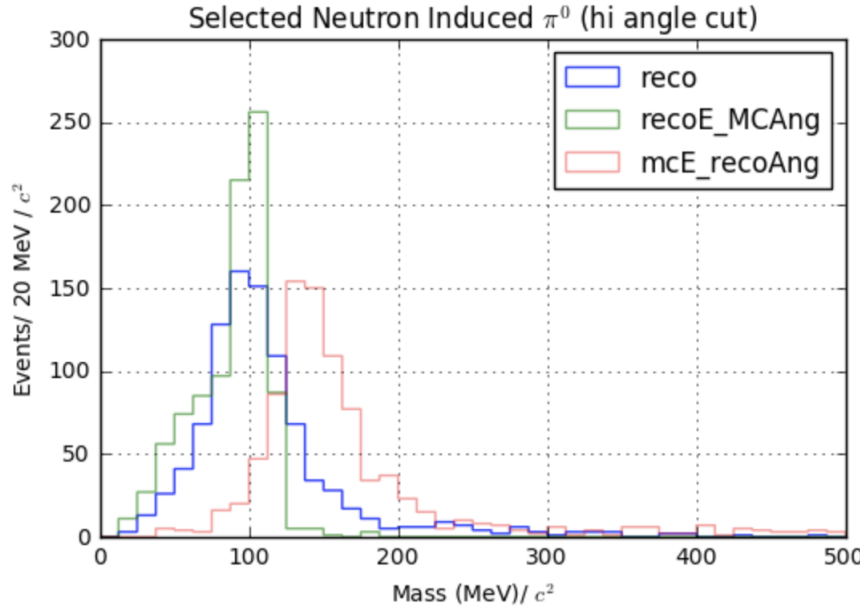


Figure 6.7: The reconstructed mass distribution is shown to highlight effects from reconstruction. First, in blue, the full reconstructed mass is shown. Second, in green, the reconstructed mass is calculated using the true angle. Third, in red, the reconstructed mass is calculated using the true energy.

the π^0 's are produced nearly at rest with both showers having similar energies. Most importantly the showers are produced nearly back to back. Without having a well defined vertex, sometime the reconstruction will identify the angle as being close to zero. Being that there is a minimum opening angle cut some of the events are lost from this effect. At high momentum, many of the showers are boosted to small opening angle which we see a similar effect in the loss of efficiency.

6.6 Single π^0 cosmic sample

The MicroBooNE cosmics Monte Carlo is generated by CORSIKA(COsmic Ray Simulation for KAscade) v-7.4003[?] CORSIKA simulates particles coming from a wide range of interactions initiated by cosmic ray particles in the upper atmosphere. The simulation is robust and accounts for various input parameters such as, longitude and latitude, elevation,

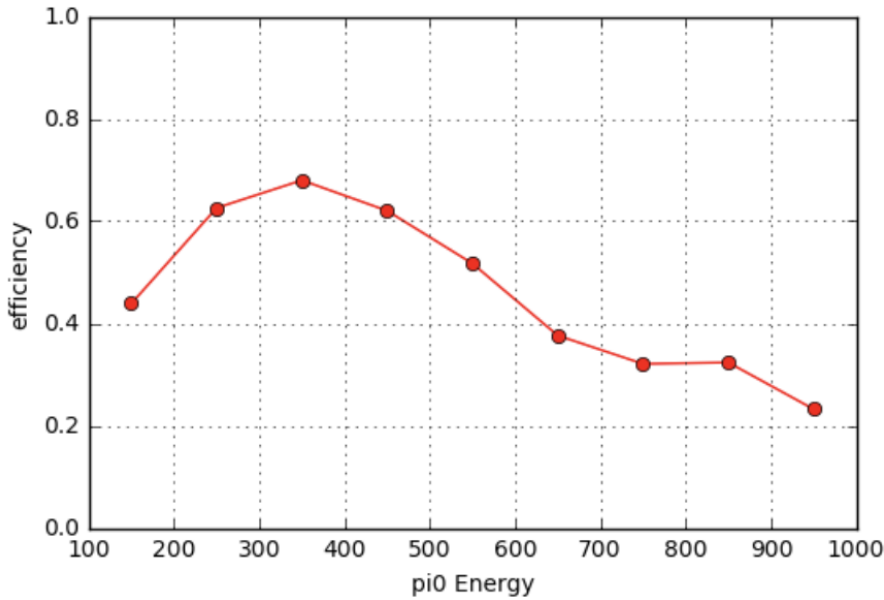


Figure 6.8: The plot shows the π^0 reconstruction efficiency for π^0 's over a 1000-10,000 MeV energy range. The reconstruction efficiency peaks around 350 MeV which conveniently is around the production energy for cosmic π^0

and the earth's magnetic field. The particles are simulated over a large region above the detector complex but only particles that travel through the detector cryostat volume are kept. The passage of these particles simulated by the GEANT4 package. Cosmic rays that do not travel through the cryostat have a low likelihood of producing secondary or tertiary particles that enter the detector TPC volume[?]

In one MicroBooNE drift window(2.3ms) there are on average 6 cosmic muons. The muons do not directly contribute to many EM-showers but sometimes pass through an EM-shower from another particle. For MicroBooNE, the vast majority of muons are through going and do not lead directly to any method of π^0 production.

Various other particles such as, protons, neutrons, and charged pions enter the TPC volume and may produce π^0 's. A distribution of π^0 production process is shown in Figure 6.9. Nearly half of the π^0 's produced in the MicroBooNE TPC are produced through a neutron inelastic scattering.

In total, 100K corsika truth events were produced to constrain production rates for signal and background. From that, a random sample of $\tilde{10}$ K events were ran through the wire-cell imaging reconstruction. Additionally, a signal sample of $\tilde{1.2}$ K was produced and reconstructed through the wire-cell imaging. *The exact rates will be discussed in Chapter 7.

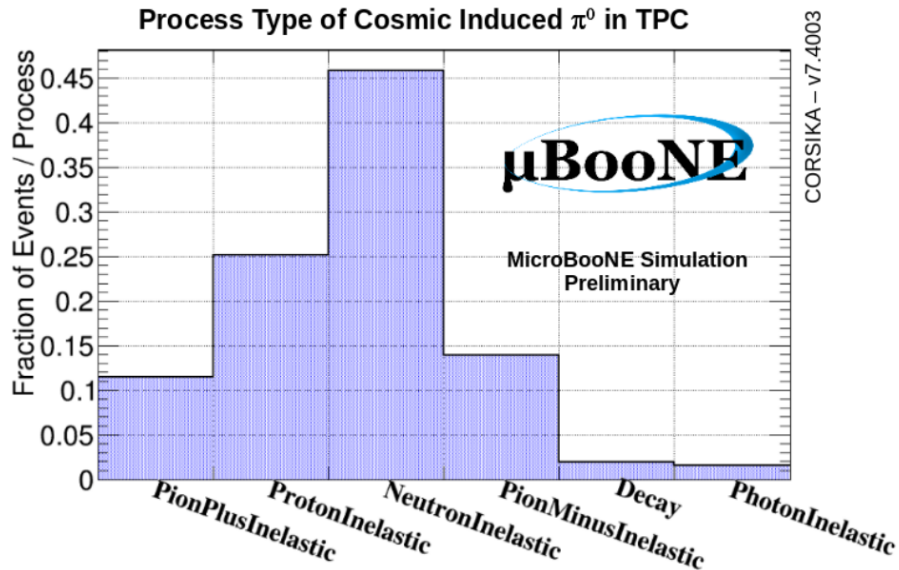


Figure 6.9: Physical process for cosmic π^0 that decay inside the TPC.

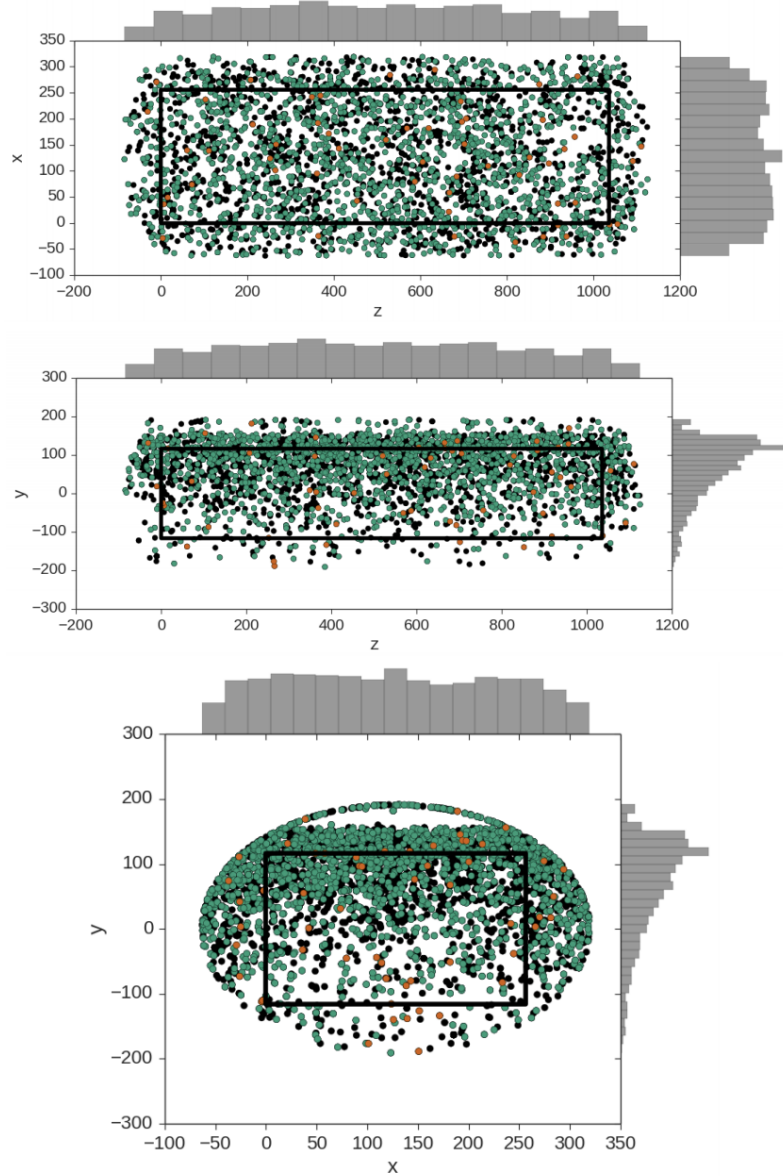


Figure 6.10: These plots show the decay point of actual cosmic π^0 's throughout any time in the 4.8 ms window. The green points represent neutron induced π^0 's, the orange represent photon induced π^0 's, and the black represent a π^0 that was produced from a charged particle. In each plot the black box is to represent the entire TPC dimensions not including fiducial cuts. Note that this is a stacked scatter plot with ordering; charged particle(black), photon(orange), neutron(green)

884 Chapter 7

885 Results

886 The goal of this study primarily two fold. The first goal is to highlight a different technique
887 to reconstruct π^0 and EM-showers in an LArTPC. To best showcase this reconstruction
888 technique we will focus on reconstructing π^0 's that are induced from a single neutron. In
889 many instances, neutral induced interactions do not have a vertex. This typically would
890 pose a challenge for traditional techniques. The second goal is to measure and compare
891 the cosmic ray neutron induced $1-\pi^0$ production rate in the MicroBooNE detector. This
892 reconstruction technique is well suited for this type of analysis.

893 This section will address results from both Monte Carlo and actual MicroBooNE cosmics
894 data. The be clear, we will define our signal to be events that produce 1 and only 1 neutron
895 induce single π^0 events inside the TPC fiducial volume. For this analysis the fiducial volume
896 is defined from: X [0,256] , Y[-116,116], Z[400,800]. We also restrict our bounds to events
897 that happen in 1 drift window as defined in section ??

898 7.1 Monte Carlo Simulation

899 A sample of 100k Corsika events were generated to simulate cosmic events in the given
900 fiducial volume cuts. One event corresponds to 1 MicroBooNE readout frame. From the
901 total sample we find that 1.43% are signal. The remaining background is divided into 5
902 categories: 1. proton induced events that produce $1\pi^0$ either inside or outside the fiducial
903 volume, 2. neutron induced events that are produced outside the fiducial volume , 3. Events

Table 7.1: Cosiska MC rates

Neutron induced 1 π^0	1,255
Neutron induced 1 else π^0	13,434
Proton induced 1 π^0 outsize	5,038
Other induced 1 π^0	9,530
no 1 π^0 or multi π^0	61,040

that produce 1 π^0 either inside or outside the fiducial volume not coming from a proton or neutron, 4. Multi π^0 produced either inside or outside the fiducial volume, 4. Events that do not contain any π^0 . Table 7.1 shows the corresponding counts from the 100K Corsika sample.

As mentioned in section 7.1., the cosmic Monte Carlo sample was comprised of scaled 90,297 Coriska truth events. This scaled is the proper scaling to account for the enhanced signal sample of 1255. This maintains the true signal rate of 0.0139% from the cosmic sample. There are a total of 443 events that pass the cuts made in section 6. This corresponds to a signal efficiency of 35.9%. A plot for the reconstructed mass is shown in figure 7.1. The mass peak, which is supposed to be around $135\text{MeV}/c^2$, is centered around $100\text{MeV}/c^2$ due to the missing energy.

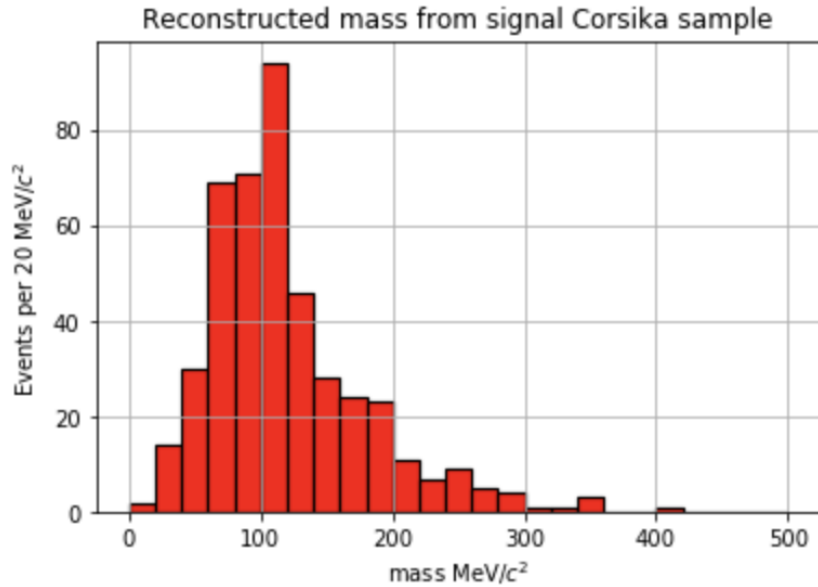


Figure 7.1: signal mass.

915 A background only sample, consisting of 8,720 randomly sampled background events
 916 were processed through wire-cell imaging and the reconstruction. This
 917 number was then scaled by 0.0147% to obtain an absolute background value relative to
 918 the enhanced signal sample. This scaling represents a new total of 90,297 events. After
 919 the sample set of cuts were applied a scaled total of 2121 selected. This corresponds to
 920 a to a background rate of 2.3%. Ultimately resulting in a signal:background of 0.21 (
 921 Approximately 1 : 5.6). A plot of the reconstructed mass distribution for the entire
 922 background is shown in figure 7.2

923 It is important to note that the background distribution will also contain π^0 events. The
 924 background distribution as described in section 7.1 is plotted in figure ?? The distribution
 925 should also have some well reconstructed π^0 . For this analysis, since we did not require the
 926 use of a vertex there is a sizable portion of background that are actual reconstructed π^0 .
 927 This comes from two primary effects both of which are products of how the reconstruction
 928 criteria is defined. The first effect is part of the $\bar{\pi}^0$ group. Many of the events are actual
 929 π^0 particles but reconstructed out side of the fiducial volume. The second effect is in the
 930 remaining π^0 groups which obviously contains at least one π^0 . Being that we remove as

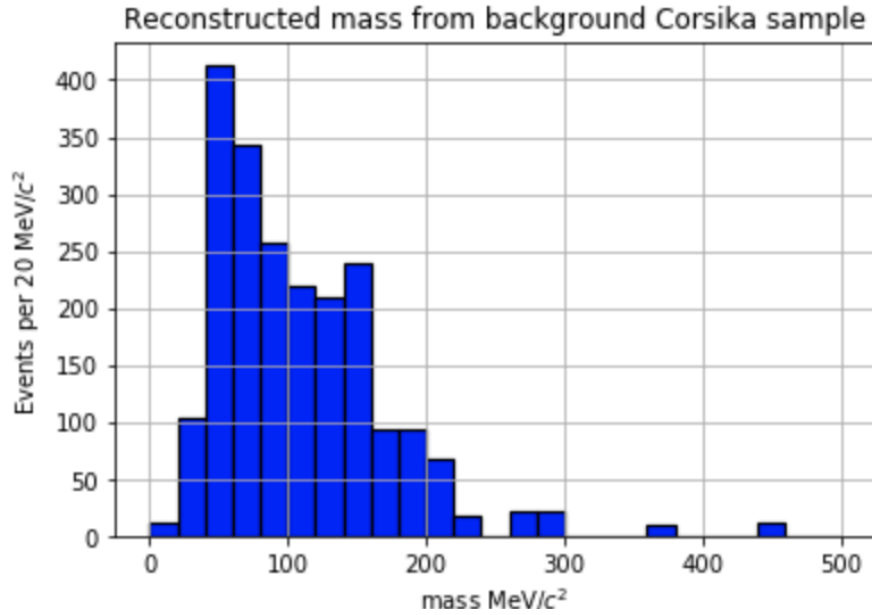


Figure 7.2: Background mass.

many track as possible, Many proton and charged pion tracks are removed. The in eyes of the selection process a proton or charged pion induced π^0 event has a near identical topology to the signal.

7.2 Data

The same background cuts were applied to a dataset of 13,022 of beam cosmic data events that were sampled from the 'MicroBooNE Good Run List'. This is an internal list that MicroBoone generates to define when the detector is in acceptable running mode. This list takes into account various aspects of the detector such as; wire stability, argon purity, PMT response, etc. It is important to note that the data sample that is used in this thesis is only from the good run list. Doing this, assumes that any bias in the sample is averaged over for interaction type.

The mass distribution is calculated from the given 13,022 sample. There is a clear resonance from the π^0 's which is also centered below the $135 \text{ MeV}/c^2$ mass.

₉₄₄ **7.3** (

₉₄₅ MC-Data Comparison)

⁹⁴⁶ **Chapter 8**

⁹⁴⁷ **Conclusions**

Part I

948

Appendices

949